

Identifying the Transcriptional Drivers of Metastasis Embedded within Localized Melanoma



Shruthy Suresh¹, Roy Rabbie², Manik Garg³, Dianne Lumaquin^{1,4}, Ting-Hsiang Huang¹, Emily Montal¹, Yilun Ma^{1,4}, Nelly M. Cruz¹, Xinran Tang^{1,5}, Jérémie Nsengimana⁶, Julia Newton-Bishop⁷, Miranda V. Hunter¹, Yuxin Zhu⁸, Kevin Chen⁸, Elisa de Stanchina⁸, David J. Adams², and Richard M. White¹

ABSTRACT

In melanoma, predicting which tumors will ultimately metastasize guides treatment decisions. Transcriptional signatures of primary tumors have been utilized to predict metastasis, but which among these are driver or passenger events remains unclear. We used data from the adjuvant AVAST-M trial to identify a predictive gene signature in localized tumors that ultimately metastasized. Using a zebrafish model of primary melanoma, we interrogated the top genes from the AVAST-M signature *in vivo*. This identified GRAMD1B, a cholesterol transfer protein, as a bona fide metastasis suppressor, with a majority of knockout animals rapidly developing metastasis. Mechanistically, excess free cholesterol or its metabolite 27-hydroxycholesterol promotes invasiveness via activation of an AP-1 program, which is associated with increased metastasis in humans. Our data demonstrate that the transcriptional seeds of metastasis are embedded within localized tumors, suggesting that early targeting of these programs can be used to prevent metastatic relapse.

SIGNIFICANCE: We analyzed human melanoma transcriptomics data to identify a gene signature predictive of metastasis. To rapidly test clinical signatures, we built a genetic metastasis platform in adult zebrafish and identified GRAMD1B as a suppressor of melanoma metastasis. GRAMD1B-associated cholesterol overload activates an AP-1 program to promote melanoma invasion.

¹Department of Cancer Biology and Genetics, Memorial Sloan Kettering Cancer Center, New York, New York. ²Wellcome Sanger Institute, Wellcome Genome Campus, Hinxton, United Kingdom. ³European Molecular Biology Laboratory, European Bioinformatics Institute (EMBL-EBI), Hinxton, United Kingdom. ⁴Weill Cornell/ Rockefeller/Sloan Kettering Tri-Institutional MD-PhD Program, New York, New York. ⁵Biochemistry and Structural Biology, Cellular and Developmental Biology and Molecular Biology Ph.D. Program, Weill Cornell Graduate School of Medical Sciences, New York, New York. ⁶Biostatistics Research Group, Population Health Sciences Institute, Faculty of Medical Sciences Newcastle University, Newcastle upon Tyne, United Kingdom. ⁷University of Leeds School of Medicine, Leeds, United

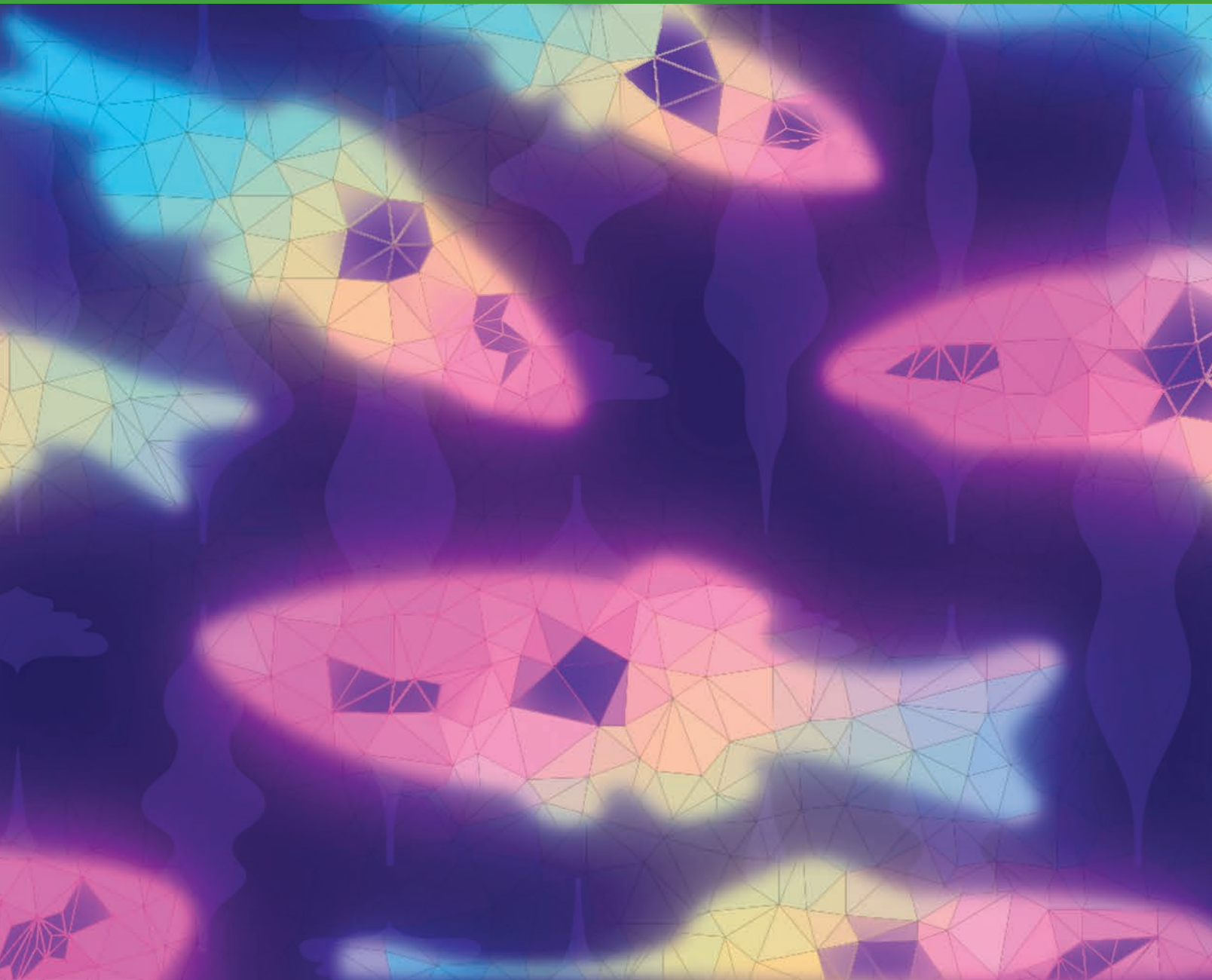
Kingdom. ⁸Antitumor Assessment Core Facility, Memorial Sloan Kettering Cancer Center, New York, New York.

Corresponding Author: Richard M. White, Department of Cancer Biology and Genetics, Memorial Sloan Kettering Cancer Center, 1275 York Avenue, New York, NY 10065. Phone: 646-888-3415; E-mail: whiter@mskcc.org
Cancer Discov 2023;13:194–215

doi: 10.1158/2159-8290.CD-22-0427

This open access article is distributed under the Creative Commons Attribution-NonCommercial-NoDerivatives 4.0 International (CC BY-NC-ND 4.0) license.

©2022 The Authors; Published by the American Association for Cancer Research



INTRODUCTION

Malignant melanomas arise from pigment cells called melanocytes or their neural crest precursors (1–3). These cells can metastasize to distant organs and drive mortality in patients (4, 5). Although significant progress has been made in melanoma biology, effective therapies targeting metastasis remain suboptimal (5). Although driver mutations in genes such as *BRAF* and *NRAS* initiate tumors (6–8), the large number of passenger alterations due to ultraviolet radiation-induced mutagenesis confounds mutational profiles in metastasis (6, 9). The tumor microenvironment with cell types such as immune cells, keratinocytes, fibroblasts, and adipocytes adds further complexity to our understanding of metastasis (10). Recent work shows that metastasis is governed less by genetic

mutations and more by epigenetic, transcriptional, and/or structural alterations (7, 8, 11, 12, 13).

Primary melanoma is a common disease, but the majority of these will not go on to metastasize. Thus, a major challenge in the field is predicting which tumors will eventually metastasize or not, as those higher-risk tumors need more careful follow-up and possible adjuvant therapy (14–17). A variety of clinical factors (i.e., Breslow thickness, ulceration, extent of tumor-involved lymph nodes) can provide such prognostic information (18, 19). Advances in imaging of these lesions, including machine learning/artificial intelligence–driven approaches, add further predictive power (20–22). However, as it is increasingly recognized that metastasis is at least partially governed by epigenetic and transcriptional changes (7, 8, 11, 12, 13),

there have been large-scale efforts into developing gene signatures of localized tumors that predict which patients will metastasize (23–29).

Despite the potential predictive power of these signatures, little is known about the mechanism by which the genes within these signatures promote metastasis. In addition, it is often not clear which transcriptional changes are drivers versus passengers in the metastatic process. In part, this is because there are few genetically tractable models of spontaneous metastasis *in vivo* (30–32). Transplantation-based models such as mouse xenografts (including cell lines or patient-derived xenografts; ref. 33) are powerful, but these represent already transformed cells, rather than primary tumors. Genetically engineered mice such as the BRAF^{V600E}; *Pten*^{-/-} and the BRAF^{V600E}; *myrAkt1*; *Cdkn2a*^{-/-} model are very useful as they recapitulate all stages of tumor development (30–32, 34). The development of ES-cell-based chimeric mice (35) has further accelerated modeling of these alterations *in vivo*, but these can still be challenging to scale up to large numbers. For these reasons, we have developed a highly scalable zebrafish model that can be used to rapidly screen for metastasis modifiers and dissect the involved mechanisms. Building off previous work showing that transgenes can be directly electroporated into the skin of adult zebrafish (Transgene Electroporation in Adult Zebrafish, or TEAZ; ref. 36), we developed a new BRAF^{V600E}; *tp53*^{-/-}; *pten*^{-/-} melanoma model that has a 25% spontaneous metastasis rate, allowing us to then readily test novel genes that modify this rate. We analyzed transcriptomics data of human melanomas to identify candidate genes whose expression from the primary or locally relapsed tumor predicted distant metastasis. Using TEAZ (36), we performed an *in vivo* metastasis screen to model these alterations and identified GRAM domain containing 1B (GRAMD1B), a cholesterol transfer protein as a novel metastasis suppressor in human melanoma. Downregulation of *GRAMD1B* is a frequent event in the tumors of melanoma patients, is associated with higher metastatic incidence, and portends poor overall survival. Our data show that *gramd1b* loss accelerates tumor growth and metastasis *in vivo*. We show that *GRAMD1B* depletion results in dysregulated cholesterol transport in melanoma cells leading to intracellular sterol accumulation and suppression of *de novo* cholesterol synthesis. This accumulated cholesterol activates an invasive transcriptional program via AP-1 transcription factor to drive metastasis. Thus, our study demonstrates the utility of our metastasis platform as a scalable system to interrogate clinical alterations and implicates *GRAMD1B* as an important gene in melanoma metastasis.

RESULTS

The AVAST-M Trial Identifies a Signature Predictive of Metastatic Relapse

To identify novel transcriptional changes that regulate metastatic dissemination, we obtained data from the AVAST-M clinical trial, the largest adjuvant study in high-risk primary melanoma (17, 23, 37). For this study, 337 patients with primary or locally advanced disease underwent bulk RNA sequencing (RNA-seq) of localized tumors along with extensive clinical follow-up to determine which patients ultimately developed

distant metastasis. Differential expression (DE) analysis was performed on the samples from patients who did or did not develop metastasis to identify a transcriptional signature that predicts metastasis (Fig. 1A; Supplementary Table S1). This revealed a total of 61 transcripts that were predictive of distant metastatic relapse (FDR-corrected $P < 0.1$). This included 41 transcripts that predicted “pan-organ” metastasis and 20 transcripts that specifically predicted metastasis to the brain (Supplementary Fig. S1; Supplementary Table S1). PANTHER pathway classification revealed that genes in this signature were enriched in pathways related to apoptosis signaling, glutamate receptor pathway, and the p53 pathway, among others (Fig. 1B). Furthermore, DAVID Gene Ontology analysis (38, 39) indicated a suppression in immune cell networks (downregulation of genes such as *PRF1*, *TRIM22*, and *KYNU*) and apoptotic signaling (downregulation of genes such as *FASLG* and *TNFRSF10A*) in patients predestined for metastasis (Supplementary Table S1 and S2). To further stratify the role of the 61 predicted metastasis suppressor genes in melanoma, we also analyzed their DNA alterations and RNA expression profiles in an independent human melanoma dataset [ref. 40; The Cancer Genome Atlas (TCGA) Firehose Legacy cohort; Fig. 1C]. Based on this analysis along with a review of the literature in melanoma, we prioritized genes that were either downregulated, deleted, or had missense mutations in this independent cohort because these types of alterations have been linked to metastasis regulation (7, 8, 11–13). This led to a prioritized list of nine candidate metastasis suppressor genes (Fig. 1C) for screening *in vivo*.

A Scalable Zebrafish Platform to Interrogate Human Clinical Gene Signatures

Transcriptional changes associated with metastasis can occur either during primary tumor evolution or after the tumors have already disseminated. In predictive scoring systems (23–28), these changes occur within early-stage tumors, necessitating genetic model systems in which these genes can be tested during *de novo* tumor initiation and evolution. To achieve this, we utilized TEAZ (36) and CRISPR–Cas9 gene editing to build a baseline metastatic melanoma model driven by expression of oncogenic BRAF^{V600E} and loss of tumor suppressors *tp53* and *pten*, common events occurring in human melanoma (refs. 31, 41; Fig. 2A). Previous work has shown that inactivation of *TP53* is relevant in human melanoma because it often occurs via loss of *CDKN2A*, although wild-type p53 can also be required for the slow-cycling state, suggesting its role can be variable depending on context (42). In our model, germline *mitfa*: BRAF^{V600E} *tp53*^{-/-} *casper* animals (41, 43) were electroporated with a MAZERATI 2X-*sgpten* (MAS2X-*sgpten*) plasmid (ref. 44; Supplementary Fig. S2A) to knockout (KO) *pten* in a melanocyte-specific manner. Introduction of this plasmid results in *mitfa* minigene expression, melanocyte rescue, expression of melanocyte-specific Cas9 and 2 single-guide RNAs (sgRNA) against *pten* (44). Loss of *pten* resulted in aggressive melanomas (70% tumor incidence) in fully immunocompetent and optically transparent animals (Fig. 2B and C). Efficient depletion of Pten in tumors was confirmed by CRISPR sequencing (Supplementary Fig. S2B) and IHC [Fig. 2D; for phospho-AKT (Serine 473); Fig. 2E]. Tumors in this model histologically resembled human melanoma, invaded into the muscle, adipose tissue

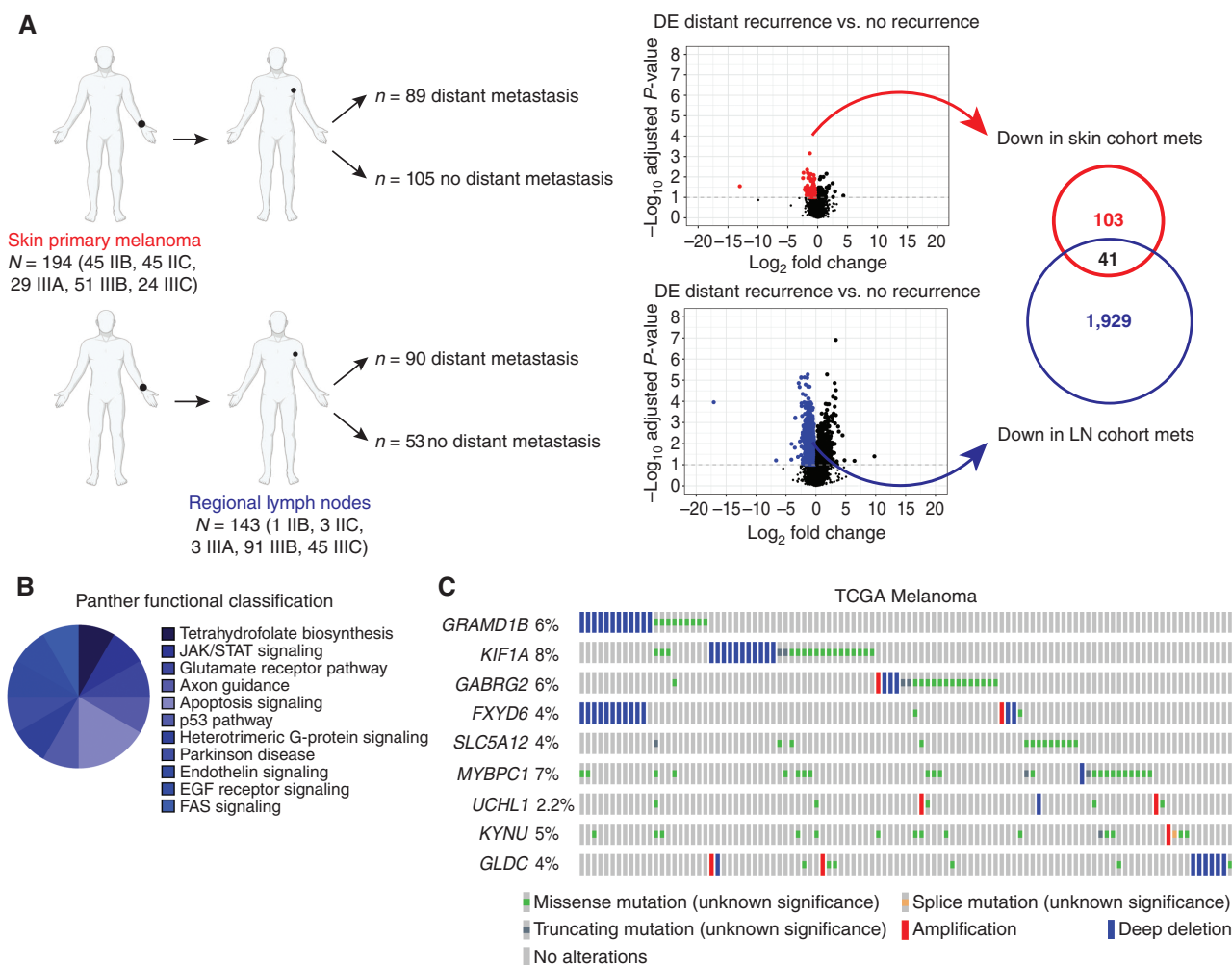


Figure 1. The AVAST-M trial identifies a signature predictive of metastatic relapse. **A**, Schematic showing the DE analysis resulting in the 41 downregulated genes associated with distant recurrence from the AVAST-M trial. The covariate-corrected DE analysis compared distant recurrence vs. no distant recurrence and was undertaken separately on primary melanomas ($n = 194$) and regional lymph node (LN) tumors ($n = 143$). Volcano plot showing, for each gene, the $-\log_{10}$ FDR-corrected P value (y -axis) and the corresponding log-fold change estimate within the DE analysis (x -axis). The (predominant) downregulated genes with an FDR-corrected $P < 0.1$ are color-coded (red dots indicate genes derived from skin primary melanomas; blue dots indicate genes derived from regional lymph node tumors). The intersecting (41) downregulated genes were selected for further testing. List of genes in Supplementary Table S1. mets, metastases. **B**, PANTHER pathway analysis of AVAST-M genes represented as a pie graph. **C**, Alteration frequency of candidate genes in the TCGA melanoma cohort (Firehose Legacy, $n = 287$). Top altered genes are plotted to display deep deletions, missense mutations, and amplifications.

and spontaneously metastasized to distal sites in 25% of animals (Fig. 2E and F). Because we aimed to perform an *in vivo* loss-of-function screen for the AVAST-M genes, we first assessed if we could model additional CRISPR-induced loss-of-function events in this system. As a proof of principle, we knocked out *slc45a2* (*alb*) gene in a melanocyte-specific manner (Supplementary Fig. S2C), which leads to impaired melanin synthesis in cells but should otherwise be neutral. Consistent with this, loss of *alb* resulted in tumors devoid of melanin (Fig. 2G and H). Moreover, CRISPR sequencing of the KO tumors revealed efficient genome editing at the *alb* locus (Supplementary Fig. S2D). Thus, this serves as proof of principle that our system can reliably model loss-of-function alterations *in vivo*. Finally, we further improved upon the efficiency of the system by electroporation of multiple smaller plasmids (Supplementary Fig. S2E) rather than the larger

MAZERATI plasmid. This multiplasmid approach led to an ~ 8 -fold increase in melanocytes transformed (Supplementary Fig. S2F) and markedly accelerated tumor initiation (Supplementary Fig. S2G and S2H). In this model, animals developed melanomas within ~ 6 weeks that metastasized within ~ 10 weeks, making this platform ideal for screening.

An *In Vivo* Screen Identifies GRAMD1B as a Metastasis Suppressor

Zebrafish orthologs of the AVAST-M candidate genes were retrieved from the Zebrafish Information Network (ZFIN; ref. 45), and 4 sgRNAs per gene were cloned into a MITF GFP 2X sgRNA plasmid. A TEAZ-based screen of these genes was performed using the above metastasis platform (Fig. 3A). Fluorescence imaging was used to quantify primary tumor area and metastatic burden over time (Fig. 3B and C). Among

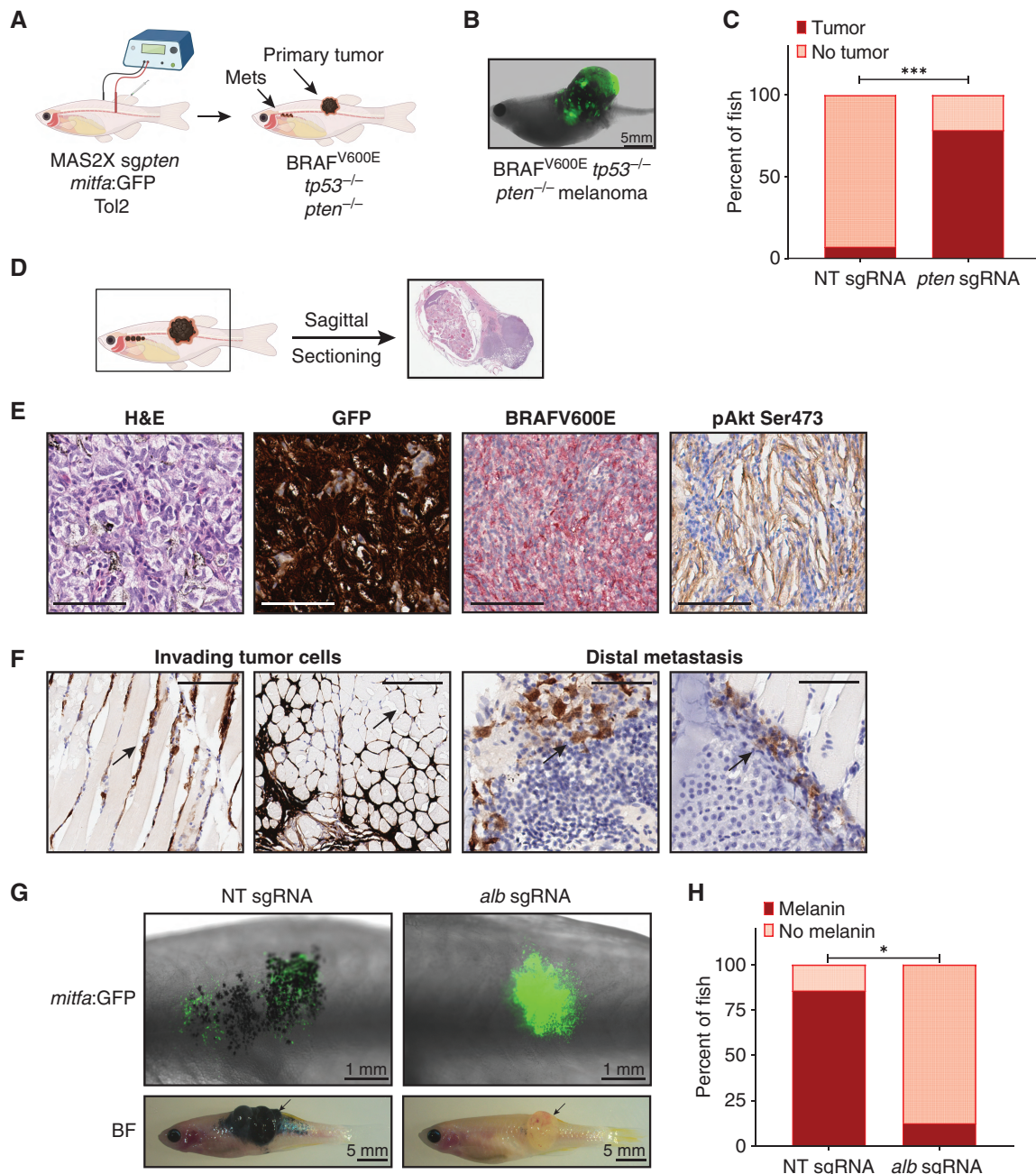


Figure 2. A TEAZ platform to screen for metastasis modulators *in vivo*. **A**, Generation of a baseline BRAFV600E *tp53*^{-/-} *pten*^{-/-} metastatic melanoma model using TEAZ. MAZERATI 2X (MAS2X) *sgpten* plasmid was coelectroporated with a *mitfa*:GFP plasmid to generate loss of Pten in a melanocyte-specific manner. mets, metastases. **B**, Representative fluorescent image of an adult zebrafish with a BRAFV600E *tp53*^{-/-} *pten*^{-/-} tumor 16 weeks after TEAZ. **C**, Quantification of tumor incidence in animals expressing a nontargeting (NT) sgRNA or *pten* sgRNAs represented as percent of fish with tumors. Fisher two-sided t test was performed on data from *n* = 3 independent experiments. ***, *P* = 0.003. **D**, Sagittal sectioning of animals with melanomas for IHC. **E**, Histology of BRAFV600E *tp53*^{-/-} *pten*^{-/-} melanomas demonstrating tumor cell expression of GFP, BRAFV600E, and activated Akt signaling. Scale bar, 60 μ m. H&E, hematoxylin and eosin. **F**, IHC staining for GFP in muscle (left images) and kidney marrow (right images) of animals bearing BRAFV600E *tp53*^{-/-} *pten*^{-/-} showing the presence of invading tumor cells (scale bar, 100 μ m) and distal metastasis (scale bar, 60 μ m), respectively. Arrows indicate metastatic tumor cells. **G**, Representative images of animals with NT or *Alb* KO melanomas at 6 weeks after TEAZ (top, fluorescent GFP imaging at 25 \times) and 12 weeks after TEAZ (bottom, brightfield image at 3.5 \times). Tumor is indicated by a black arrow in each group. Scale bar on the graph. BF, Brightfield. **H**, Quantification of the presence of melanin in animals expressing a NT sgRNA or *alb* sgRNAs represented as percent of fish with melanin. Fisher two-sided t test was performed on data from *n* = 3 independent experiments. *, *P* < 0.05.

the 9 candidates, loss of *gramd1b* (GRAM Domain Containing 1B) led to significantly increased tdTomato⁺ primary tumor area at 4 and 8 weeks after TEAZ (Fig. 3B). Subsequent validation experiments using larger cohorts of animals

confirmed that *gramd1b* functioned as a tumor suppressor *in vivo* (Fig. 3D). Loss of *gramd1b* was confirmed by surveyor assays (Supplementary Fig. S3A) and real-time PCR (Supplementary Fig. S3B). Because *GRAMD1B* was identified as a

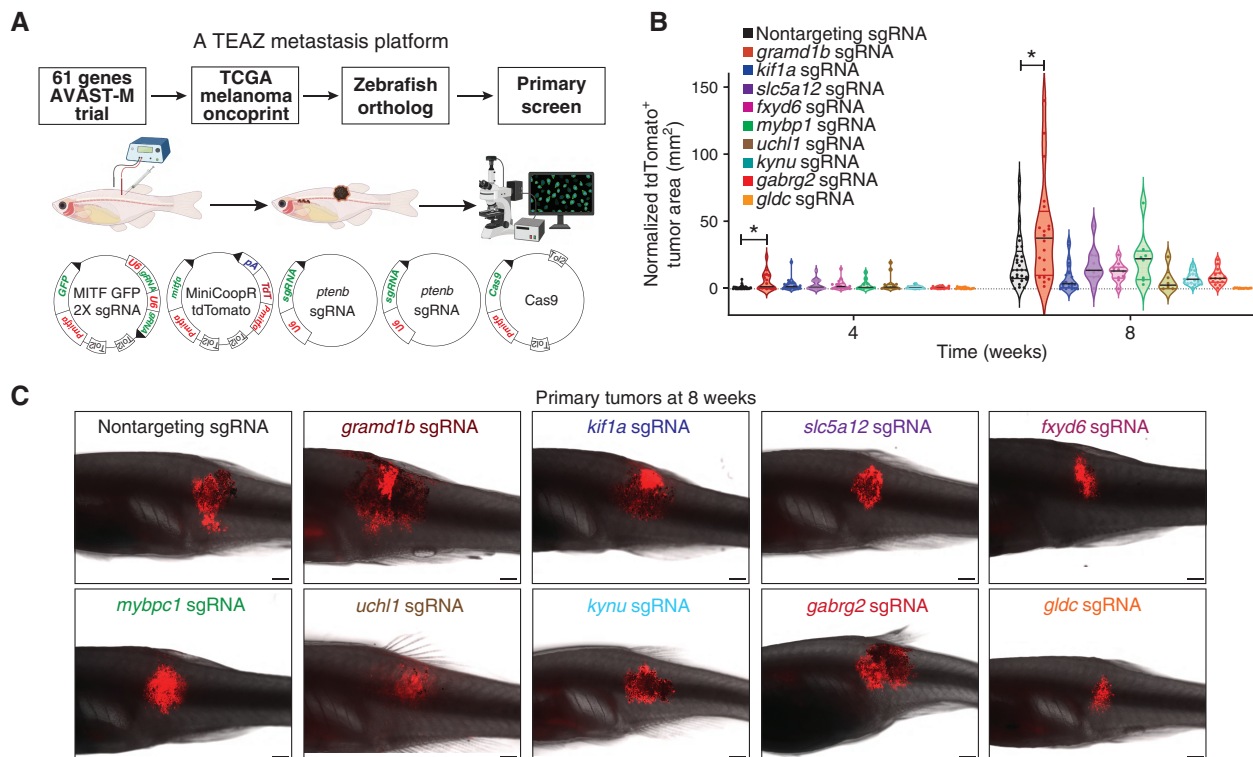


Figure 3. An *in vivo* screen identifies GRAMD1B as a metastasis suppressor in melanoma. **A**, Strategy for *in vivo* metastasis screen. Zebrafish orthologs for candidate genes were obtained and MITF GFP 2X sgRNA pools expressing 4 sgRNAs per candidate were co-electroporated with the multi-plasmid mix to induce metastatic melanoma. Candidates from the primary screen were assessed for their ability to modulate metastasis via fluorescent imaging of areas separate from the primary tumor. See Methods for details. **B**, Quantification of tdTomato⁺ primary tumor area in animals expressing nontargeting (NT) sgRNA or sgRNA pools against candidates at 4 and 8 weeks after TEAZ. Data were obtained from $n = 3$ independent experiments, and all data points were normalized to NT sgRNA tumors at week 4. Error bars, SD; Mann-Whitney test was used to compare ranks between tumor area of candidates vs. NT sgRNA at each time point. *, $P = 0.013$. **C**, Representative images showing tdTomato⁺ melanomas from animals expressing a NT sgRNA or candidate sgRNAs at 8 weeks after TEAZ. Scale bar, 1 mm. (continued on next page)

putative metastasis suppressor from human melanoma samples, we assessed if *gramd1b* KO tumors had altered metastatic potential. Fluorescent imaging of animals at 12 weeks after TEAZ (Fig. 3E) revealed that animals with *gramd1b* KO tumors had increased visceral metastasis (to the kidney marrow), compared with controls (Fig. 3F). Furthermore, IHC for tdTomato confirmed extensive infiltration of metastatic tumor cells into the kidney marrow of animals with KO tumors (Fig. 3G). Animals with KO tumors had significantly increased metastatic incidence as well as burden relative to control tumors (Fig. 3H and I). Interestingly, loss of two other genes, *kif1a* and *gabrg2*, significantly increased metastatic burden in animals without affecting primary tumor growth (Supplementary Fig S4A and S4B), which will be investigated in the future. Collectively, these data demonstrate that our metastasis platform can be used to screen clinical alterations and uncover novel metastatic modulators in human melanoma.

GRAMD1B Is a Metastasis Suppressor in Human Melanoma Cells

Because *gramd1b* loss in zebrafish had such a pronounced effect on metastasis of zebrafish melanoma cells, we sought to investigate its role in human melanoma. Analysis of the AVAST-M melanoma cohort samples showed that patients with low GRAMD1B expression had poor overall and progression-free

survival in the AVAST-M melanoma cohort (Fig. 4A; Supplementary Fig. S5A). GRAMD1B expression was significantly associated with survival after correcting for clinical correlates such as sex, age, stage, and treatment in the AVAST-M melanoma cohort and an independent AVAST-M lymph node cohort (Fig. 4B; Supplementary Fig. S5B). To further validate its role in human melanoma, we analyzed three independent patient cohorts. In the skin cutaneous melanoma cohort (TCGA, $n = 287$) and the UCLA Metastatic Melanoma cohort ($n = 38$), deep deletions and missense mutations in GRAMD1B are frequent events (ref. 40; Supplementary Fig. S5C and S5D). In the Leeds Melanoma Cohort ($n = 666$; ref. 24), which includes stage I-III tumors, low GRAMD1B expression predicted poor survival in thicker tumors (Breslow > 3 mm; Fig. 4C) as well in \geq stage IIB tumors regardless of Breslow thickness. These clinical data encouraged us to further focus on its functional role. GRAMD1B belongs to the GRAM domain 1 family of proteins (consisting of GRAMD1A, GRAMD1B, and GRAMD1C) and encodes a cholesterol transfer protein that mediates nonvesicular transport of cholesterol within cells (46, 47). Although GRAMD1B has been shown to transport cholesterol in mouse adrenal tissue and human embryonic kidney cells (46, 48), the biological significance of this protein in melanoma cells and cancer in general has not been well explored. To better understand its role in melanoma, we performed RNA-seq in human SKMEL2

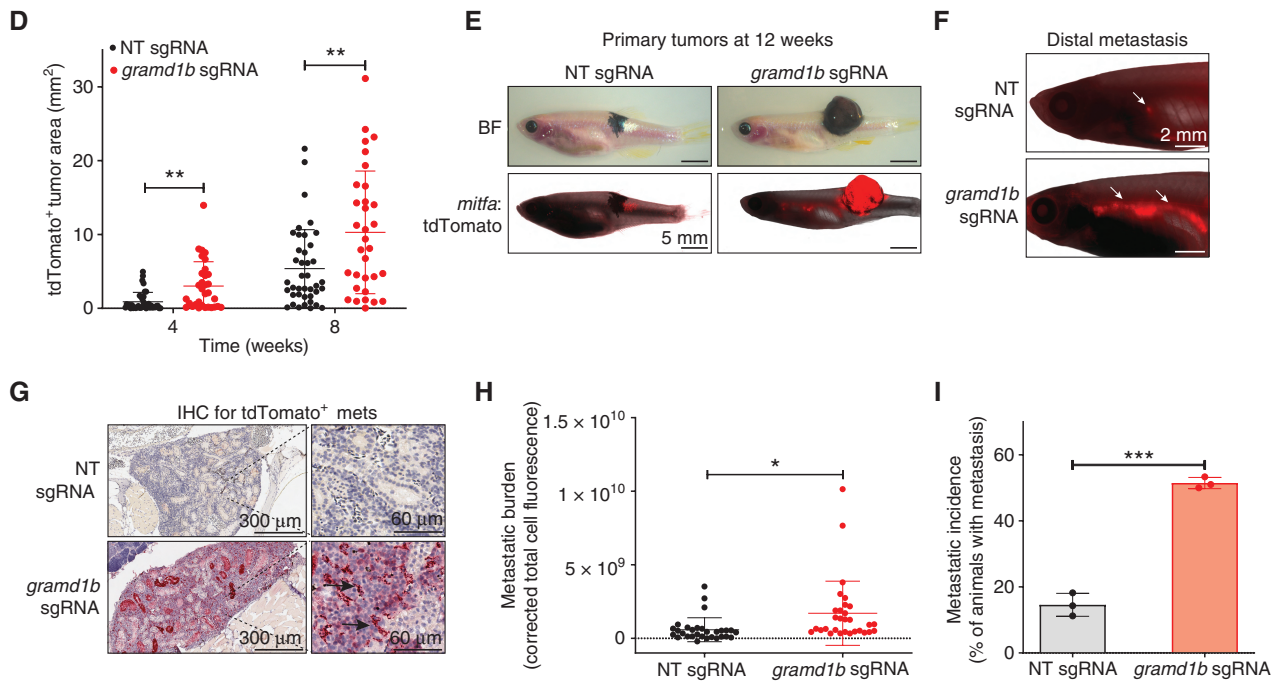


Figure 3. (Continued) **D**, Quantification of $tdTomato^+$ primary tumor area in a validation cohort of animals expressing NT sgRNA or *gramd1b* sgRNAs at 4 and 8 weeks after TEAZ. Data are pooled from $n = 4$ independent experiments. Error bars, SD; Mann-Whitney test was used to compare ranks between tumor areas of *gramd1b* sgRNA vs. NT sgRNA at each time point to obtain; **, $P = 0.001$ at 4 weeks; **, $P = 0.007$ at 8 weeks. **E**, Representative brightfield and fluorescent images for $tdTomato$ showing animals bearing tumors expressing NT sgRNA or *gramd1b* sgRNAs at 12 weeks after TEAZ. Scale bar, 5 mm. BF, Brightfield. **F**, Representative fluorescent image of $tdTomato^+$ distal metastasis (white arrows indicate metastatic cells) in the kidney marrow of animals expressing NT or *gramd1b* sgRNAs. Scale bar, 2 mm. **G**, IHC validation of $tdTomato^+$ metastatic tumor cells (black arrows) in kidney marrow of an animal expressing *gramd1b* sgRNAs. Scale bars indicated on image. mets, metastases. **H**, Quantification of metastatic burden in animals expressing NT or *gramd1b* sgRNAs represented as corrected total cell fluorescence (integrated density, sum of values of $tdTomato$ pixels in image) at 12 weeks after TEAZ. Data are pooled from $n = 4$ independent experiments. Error bars, SD; Welch t test was used to test statistical significance. *, $P = 0.0122$. **I**, Quantification of metastatic incidence in animals with NT or *gramd1b* KO melanomas expressed as % of fish with metastasis at 12 weeks after TEAZ. Data are pooled from $n = 4$ independent experiments. Error bars, SD; Welch t test was used to assess statistical significance. ***, $P = 0.0005$.

cells to identify differentially expressed genes in GRAMD1B KO cells (Fig. 4D). Introduction of *GRAMD1B* sgRNA led to potent target depletion (Fig. 4D), whereas transcript levels of *GRAMD1A* and *GRAMD1C* remained unaltered (Supplementary Fig. S5E). Gene set enrichment analysis (GSEA) identified epithelial-to-mesenchymal transition (EMT) as one of the top enriched pathways in the KO cells (Fig. 4E). Specifically, there was a significant upregulation in EMT genes such as *SERPINE2*, *CCN2*, *COL12A1*, and *MMP1* in the KO cells, previously reported to promote metastasis (refs. 49–54; Fig. 4F). This indicated that GRAMD1B loss may promote metastasis not only in zebrafish melanoma cells but also in human melanoma. To further functionally test this, we knocked out GRAMD1B in a panel of human melanoma cell lines (SKMEL2, A375, and A2058) using lentiviral expression of Cas9 and sgRNAs against *GRAMD1B*. Although we saw no defect in proliferation (Supplementary Fig. S6A–S6C), we found a significant increase in invasion in a Matrigel-coated transwell invasion assay in all 3 cell lines (Fig. 4G; Supplementary Fig. S6D and S6E). Similar results were seen upon shRNA-mediated knockdown of *GRAMD1B* in SKMEL2 cells (Supplementary Fig. S6F). Although GRAMD1B loss promoted invasiveness through Matrigel, the migratory ability of these cells in the absence of Matrigel was not altered (Supplementary Fig. S6G), suggesting the metastatic phenotypes may be specific to its function in ECM degradation and extravasation. Consistent with this, we performed qRT-PCR and

observed an upregulation of multiple *MMP* genes, which are known to cleave ECM proteins, upon GRAMD1B KO in these 3 different human melanoma cell lines (Supplementary Fig. S6H–S6J). Finally, to test if *GRAMD1B* depletion alters the metastatic ability of human melanoma cells *in vivo*, we generated doxycycline (dox)-inducible NT or *GRAMD1B* shRNA SKMEL2 cells expressing TurboRFP and performed a tail-vein metastasis assay in NSG mice (Fig. 4H). We observed that *GRAMD1B* depletion potentially increased metastasis to the liver (RFP⁺ tumor cells in the livers of 100% of animals) and lung (RFP⁺ cells in the livers of 90% of animals) compared with an NT control (no RFP⁺ tumor cells detected) within 3 weeks (Fig. 4I). Histologic examination via hematoxylin and eosin (H&E) staining confirmed the presence of metastatic nodules in the liver and lungs (Fig. 4J). Color deconvolution was performed to separate hematoxylin stains in mouse livers to quantify tumor-positive liver area. This analysis revealed that *GRAMD1B* depletion led to increased metastatic burden in the liver (Fig. 4K). Taken together, these data demonstrate that GRAMD1B suppresses the invasiveness of human melanoma cells *in vitro* and metastasis *in vivo*.

GRAMD1B Loss Leads to Cholesterol Overload in Melanoma Cells

GRAMD1B represents a newly reported cholesterol transporter that mediates the nonvesicular transfer of accessible cholesterol from the plasma membrane (PM) to the endoplasmic

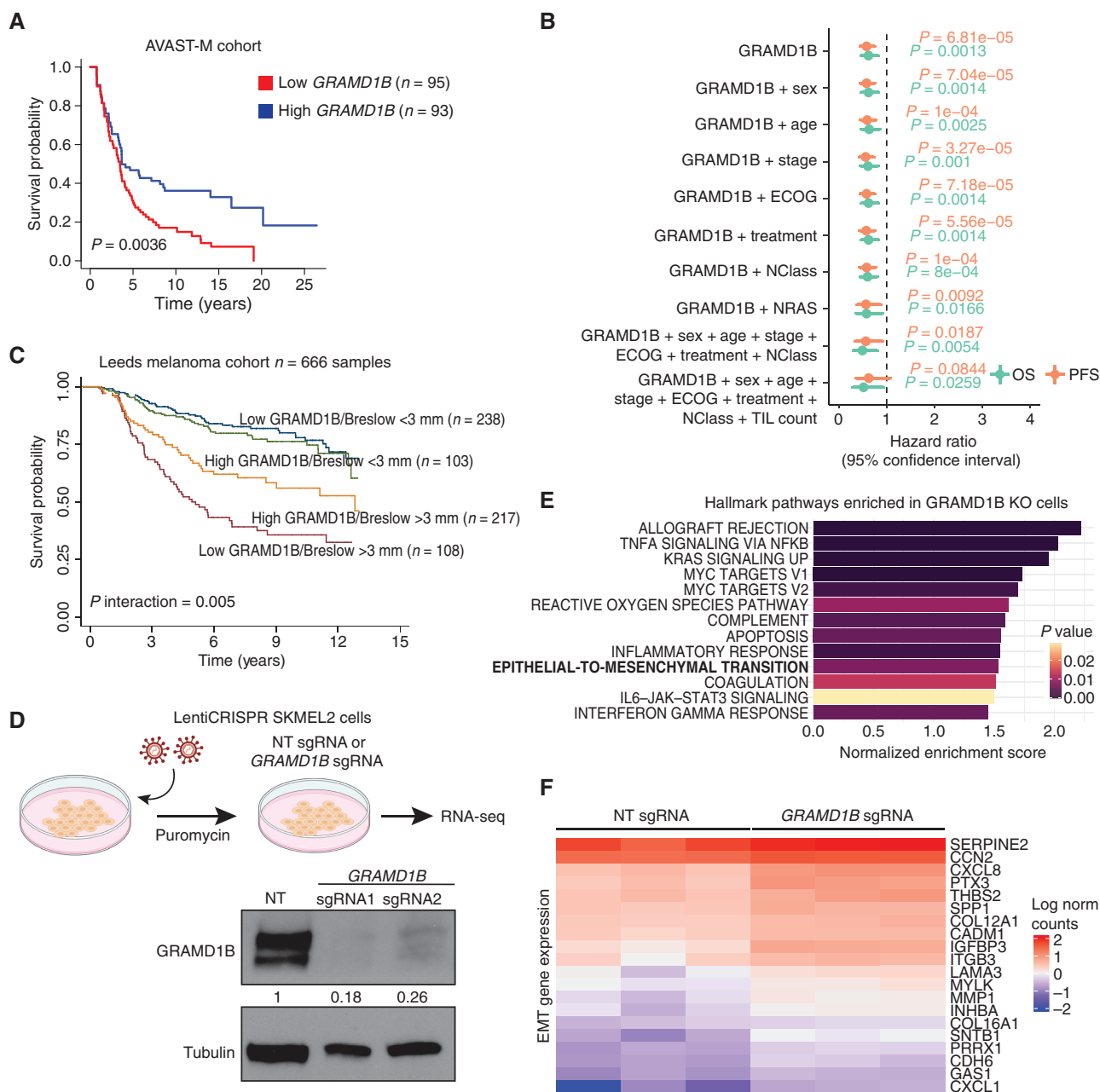


Figure 4. GRAMD1B is a metastasis suppressor in human melanoma. **A**, Kaplan-Meier survival plots comparing overall survival (OS) probabilities (Y-axis) as a function of time in years (x-axis) in patients with low ($n = 95$) and high ($n = 93$) GRAMD1B expression based on median GRAMD1B expression split in the AVAST-M melanoma cohort. A log-rank test comparing the survival distributions of both groups is indicated with a P value. **B**, Forest plot indicating the hazard ratio (HR) estimates related to GRAMD1B expression when predicting OS (green) and progression-free survival (PFS; orange) by means of Cox proportional hazard models controlling for different clinical variables (y-axis) in the AVAST-M melanoma cohort ($n = 194$). The HR estimates are indicated by the dots at the center of the error bars; the horizontal error bars correspond to the 95% confidence intervals of the HR. The two-sided Wald t test P values corresponding to GRAMD1B expression are indicated for each model and outcome. Sex (male or female), age (as a continuous variable), stage (IIB, IIC, IIIA, IIIB, or IIIC), ECOG; Eastern Cooperative Oncology Group Performance Status (0 or 1), treatment (bevacizumab or placebo), NClass (N0, N1, N2, or N3), NRAS mutation (mutant or wild-type); TIL count, tumor-infiltrating lymphocyte count (brisk, nonbrisk or absent). **C**, Kaplan-Meier plot for melanoma-specific survival in patients with low and high GRAMD1B expression (split on median) and Breslow thickness (split at 3 mm). There is a significant interaction ($P = 0.005$) between the two factors in Cox proportional hazards risk regression. The difference between the two bottom curves has an HR of 0.56 (95% CI, 0.38–0.83). **D**, Generation of SKMEL2 cells expressing nontargeting (NT) sgRNA and GRAMD1B sgRNA for bulk RNA-seq. RNA-seq was performed on $n = 3$ biological replicates per experimental group (top). Bottom, Western blot analysis of GRAMD1B in SKMEL2 cells expressing an NT sgRNA or 2 independent sgRNAs against GRAMD1B. Tubulin served as a loading control in this and all subsequent Western blots. Quantification of GRAMD1B normalized to Tubulin and relative to NT sgRNA are in black text below the blot. **E**, Bar graph depicting top Hallmark pathways enriched in GRAMD1B KO cells plotted against the normalized enrichment score. An FDR cutoff of 0.1 was used for multiple hypothesis testing, and pathways are ranked by nominal P value. (continued on next page)

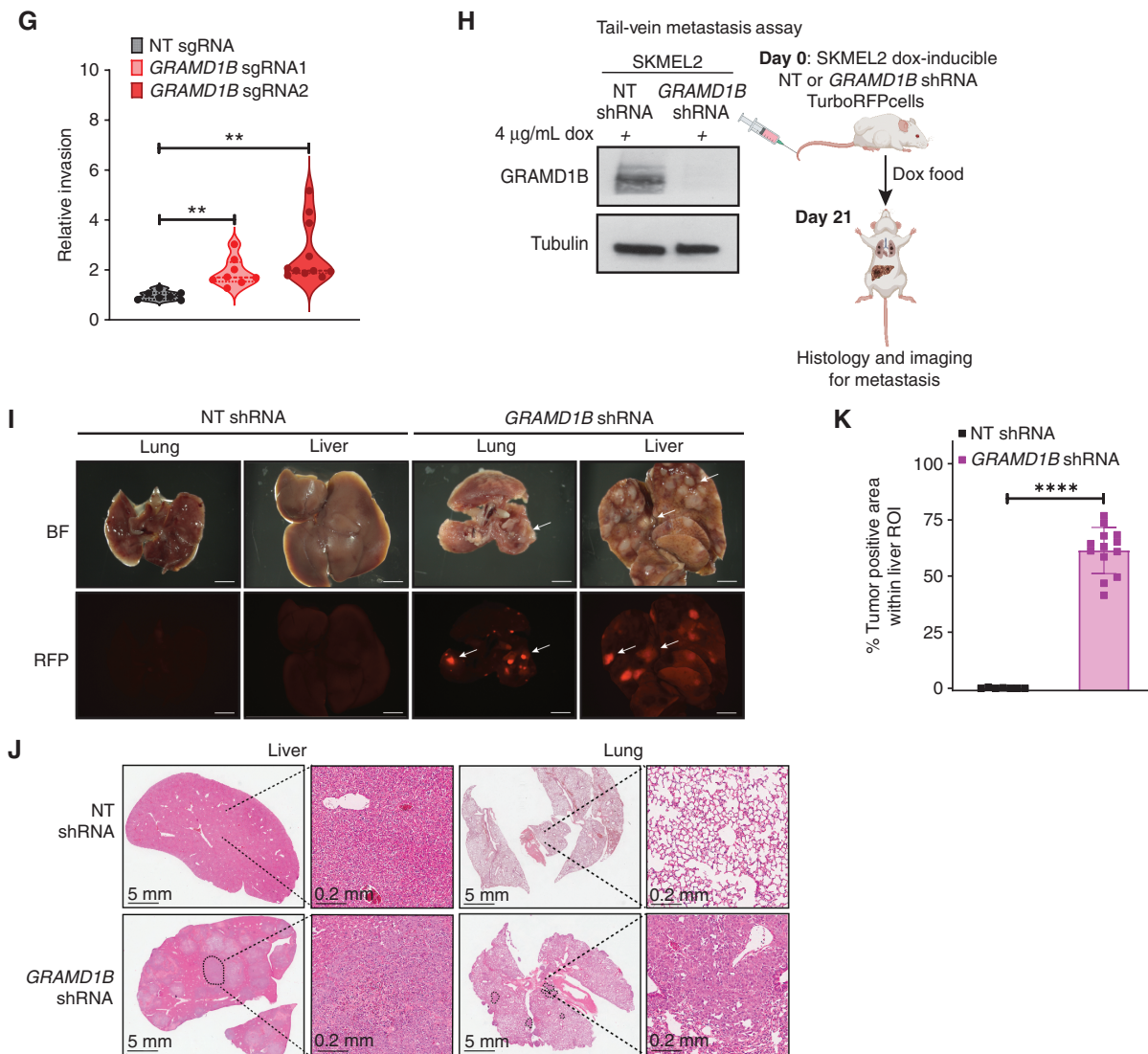


Figure 4. (Continued) F, Heat map depicting differential upregulation of EMT genes in GRAMD1B KO cells. Log₂ normalized counts of genes involved in the EMT pathway (FDR $q = 0.028$) are rescaled and plotted for NT and GRAMD1B sgRNA samples, $n = 3$ biological replicates per group. **G**, Quantification of invasiveness of GRAMD1B KO SKMEL2 cells relative to NT cells. Data represent fold change in invasion and pooled from $n = 3$ independent experiments. Invasiveness was calculated by normalizing Calcein fluorescence to the NT group. See Methods for details. Error bars, SD; two-tailed t test was used to assess statistical significance. **, $P = 0.001$ for GRAMD1B sgRNA1 vs. NT; **, $P = 0.002$ for GRAMD1B sgRNA2 vs. NT. **H**, Schematic for generation of dox-inducible shRNA cells for the tail-vein metastasis assay in mice. Left, Western blot analysis of GRAMD1B in SKMEL2 cells expressing an NT shRNA or GRAMD1B shRNA and treated with dox for 4 days. Right, schematic of tail-vein metastasis assay using these shRNA cells. **I**, Brightfield and fluorescent (RFP) images of lung and liver tissues imaged at 6 × 3 weeks after tail-vein injection of NT or GRAMD1B shRNA SKMEL2 cells. White arrows represent metastatic tumor cells. BF, Brightfield. **J**, Histology of mouse lung and liver tissues from mice injected with NT or GRAMD1B shRNA SKMEL2 cells. Scale bars, 5 mm or 0.2 mm. **K**, Quantification of metastatic burden in livers of mice injected with NT or GRAMD1B shRNA SKMEL2 cells, represented as % tumor-positive liver area. $n = 2$ animals per group, with 4–5 regions of interest (ROI) per liver lobe. Error bars, SD; Welch t test was used to assess statistical significance. ****, $P < 0.00001$.

reticulum (ER; refs. 46, 55, 56). GRAMD1B loss in mouse adrenal tissues did not affect total cholesterol levels, but led to decreased ER cholesterol, increased nuclear translocation of sterol regulatory element-binding transcription factor 2 (SREBP2), the master transcription factor regulating *de novo* cholesterol synthesis, and increased transcription of *de novo* synthesis genes (46). In contrast, another recent study reports that GRAMD1B is also required for lysosome to ER transfer of low density lipoprotein (LDL) cholesterol and that GRAMD1B knockdown leads to increased free cholesterol within cells (57). Thus, its precise role in mammalian cancer cells remains under investigation.

We analyzed our RNA-seq data and noted significant downregulation in cholesterol synthesis pathways in GRAMD1B KO cells (Fig. 5A). Mammalian cells maintain cholesterol homeostasis by tightly regulating its transport across organelles. Excess ER cholesterol binds SCAP and prevents the ER to Golgi transport of the SCAP-SREBP2 complex (58–60). This prevents proteolytic processing of active SREBP2 and results in suppression of transcription of *de novo* synthesis. Consistent with this, real-time PCR quantification confirmed the downregulation of SREBF2 as well as key *de novo* cholesterol genes such as HMGCR and HMGCS1 upon GRAMD1B loss in

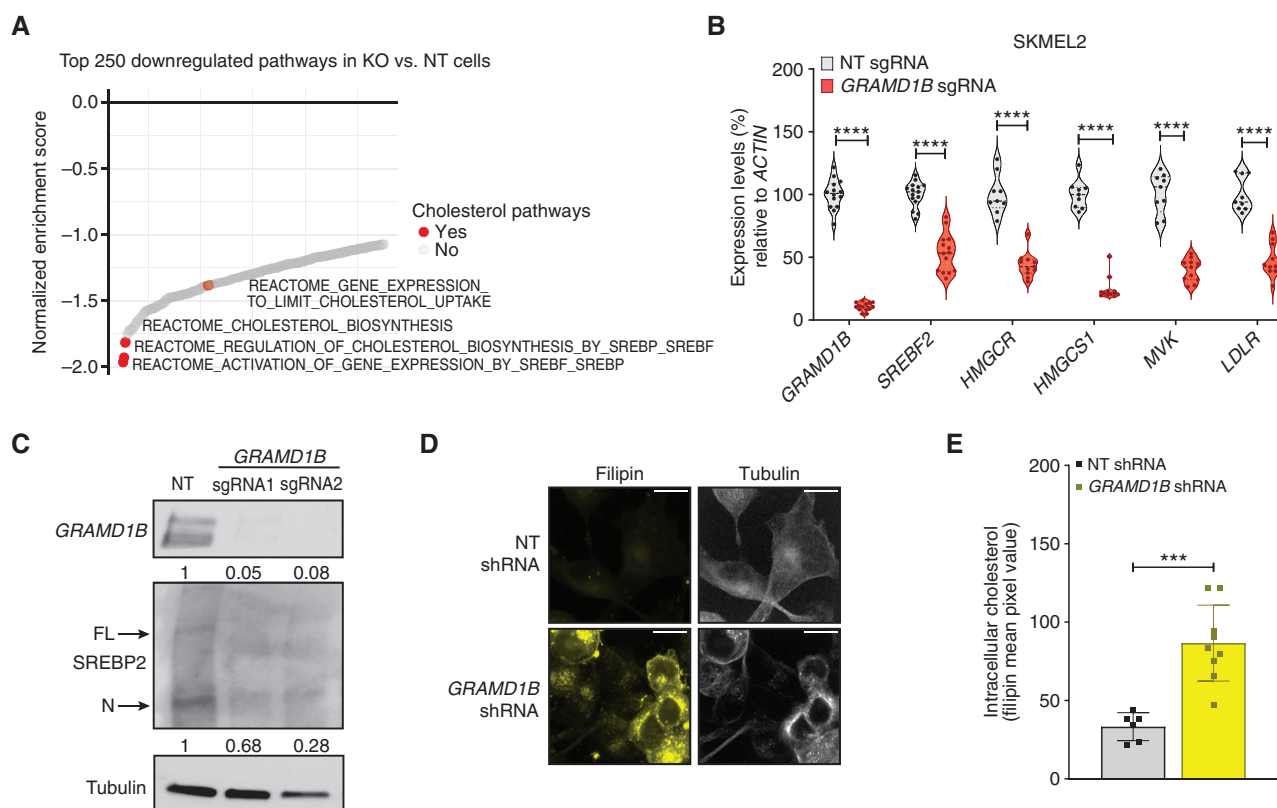


Figure 5. GRAMD1B loss leads to cholesterol overload in melanoma cells. **A**, Waterfall plot depicting top 250 downregulated pathways in GRAMD1B KO cells plotted against their normalized enrichment score. Cholesterol-related pathways are highlighted in red. **B**, Real-time PCR quantification of cholesterol synthesis genes in nontargeting (NT) and GRAMD1B KO cells. Violin plots represent the expression of genes (in %) relative to *ACTIN*. Data are pooled from $n = 3$ independent experiments. Error bars, SD; Welch *t* test was used to assess statistical significance. ****, $P < 0.00001$. **C**, Western blot analysis of full-length (FL) and nuclear (N) SREBP2 in whole-cell lysates from SKMEL2 cells expressing NT or GRAMD1B sgRNAs. Quantification of GRAMD1B and nuclear SREBP2 are shown below the blot. **D**, Representative confocal microscopy image of Filipin staining in SKMEL2 cells expressing an NT or GRAMD1B shRNA demonstrating elevated free cholesterol within GRAMD1B knockdown cells. Scale bar, 13 μm. **E**, Quantification of intracellular free cholesterol in NT and GRAMD1B shRNA cells represented as mean pixel value of Filipin intensity. Data are from $n = 3$ independent experiments. Error bars, SD; Welch *t* test was used to assess statistical significance. ***, $P = 0.0009$. (continued on next page)

both SKMEL2 cells (Fig. 5B) and A375 cells (Supplementary Fig. S7A). Similar results were obtained using both sgRNA and shRNA approaches (Supplementary Fig. S7B). Furthermore, there was a decrease in nuclear SREBP2 protein levels upon GRAMD1B loss in these cells (Fig. 5C). Our data are, therefore, suggestive of an increase in cholesterol in the KO cells, similar to what is seen by directly supplementing excess cholesterol to these cells (Supplementary Fig. S7C and S7D).

These findings led us to hypothesize that GRAMD1B loss leads to free cholesterol accumulation in melanoma cells. To test this, we used dox-inducible NT or GRAMD1B shRNA in SKMEL2 cells (Supplementary Fig. S7E) and measured cholesterol levels in these cells using two independent assays. We stained NT and GRAMD1B shRNA cells with Filipin, an endogenous cholesterol probe, and observed a striking increase in Filipin staining in GRAMD1B knockdown cells (Fig. 5D and E). We also performed cholesterol extractions in three independent human melanoma cell lines and observed an increase in free cholesterol upon GRAMD1B depletion (Fig. 5F–H). Next, to test if *gramd1b* loss leads to free cholesterol accumulation *in vivo*, we performed cholesterol extractions from transgenic zebrafish melanomas as well as the

blood of animals bearing NT or *gramd1b* KO tumors (Fig. 5I). We observed that *gramd1b* loss led to an increase in free cholesterol in tumor tissues (Fig. 5J), similar to what we saw *in vitro*. We did not see an effect on serum cholesterol levels (Fig. 5K), indicating that GRAMD1B acts at least in part in a cell-autonomous manner to regulate intracellular cholesterol levels. As most of the cholesterol in cells are located in the PM, we assessed whether this increase in free cholesterol affected PM composition and integrity. GRAMD1B knockdown did not significantly alter the abundance of choline-containing phospholipids in the cells (Supplementary Fig. S7F). To assess the consequences of GRAMD1B knockdown on membrane fluidity, we measured the lateral diffusion of lipophilic pyrene probes in NT and GRAMD1B knockdown cells. These probes undergo excimer formation upon spatial interaction at the cell membrane and exhibit change in their spectral properties compared with their monomer counterpart. We did not observe a significant change in membrane fluidity upon GRAMD1B knockdown (Supplementary Fig. S7G). Taken together, these findings suggest that GRAMD1B loss leads to free cholesterol accumulation in melanoma cells *in vitro* and *in vivo*.

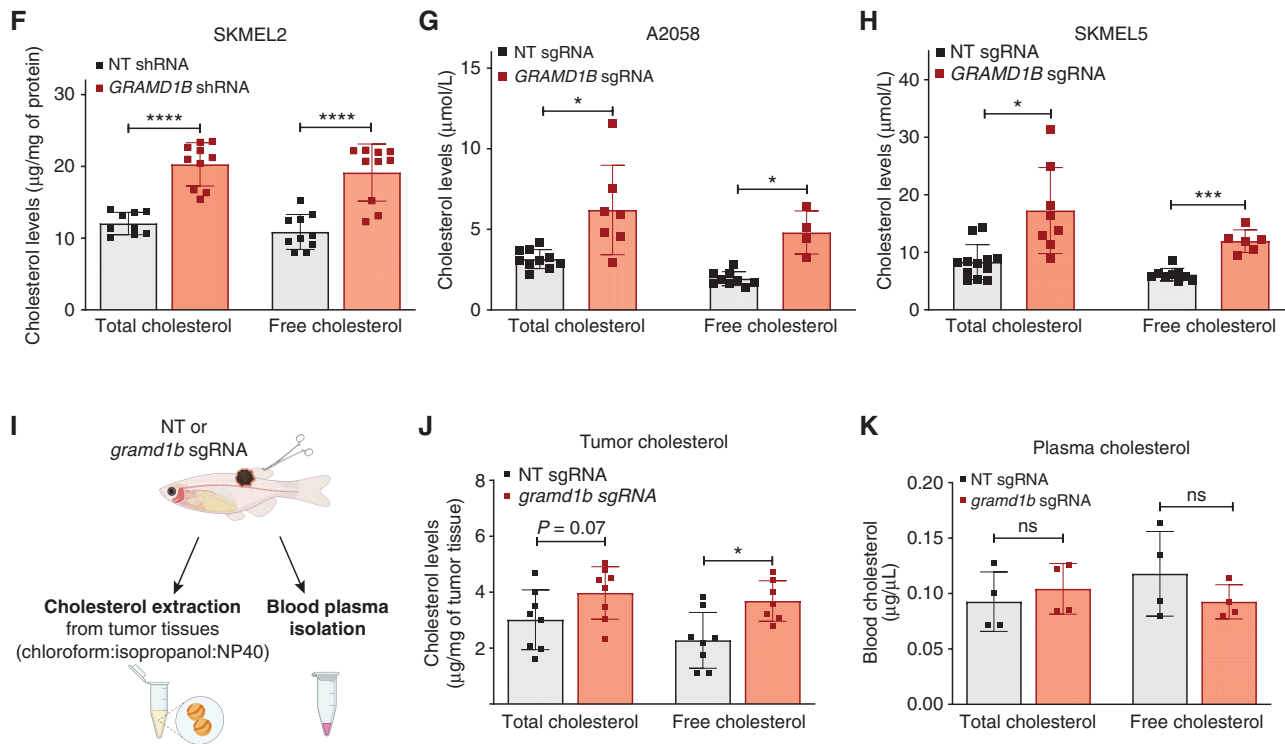


Figure 5. (Continued) **F**, Total and free cholesterol levels normalized to total protein ($\mu\text{g}/\text{mg}$) in NT and *GRAMD1B* shRNA SKMEL2 cells. Data are pooled from $n = 3$ independent experiments. Error bars, SD; Welch *t* test was used to assess statistical significance. ****, $P < 0.0001$. **G**, Total and free cholesterol levels normalized to total viable cells ($\mu\text{mol}/\text{L}$) in NT and *GRAMD1B* KO A2058 cells. Data are pooled from $n = 3$ independent experiments. Error bars, SD; Welch *t* test was used to assess statistical significance. *, $P < 0.05$. **H**, Total and free cholesterol levels normalized to total viable cells ($\mu\text{mol}/\text{L}$) in NT and *GRAMD1B* KO SKMEL5 cells. Data are pooled from $n = 3$ independent experiments. Error bars, SD; Welch *t* test was used to assess statistical significance. *, $P < 0.05$; ****, $P < 0.0001$. **I**, Schematic of extraction of blood and tumor cholesterol from animals bearing NT or *gramd1b* KO tumors. Tumor cholesterol was extracted from primary tumor tissues in chloroform:isopropanol:NP40. See Methods for details. **J**, Total and free cholesterol levels normalized to tumor weight (mg) in NT or *gramd1b* KO tumors. Data are representative of $n = 4$ independent animals per group, measured in duplicates. Error bars, SD; Welch *t* test was used to assess statistical significance. *, $P < 0.05$. **K**, Total and free blood cholesterol levels in animals bearing NT or *gramd1b* KO tumors. Data are representative of $n = 4$ independent animals per group. Error bars, SD; Welch *t* test was used to assess statistical significance. *, $P < 0.05$.

GRAMD1B-Associated Cholesterol Overload Activates the AP-1 Axis

As *GRAMD1B* loss led to an increase in free intracellular cholesterol, we hypothesized that the invasiveness of *GRAMD1B* KO cells is dependent on cholesterol accumulation. To test this, we depleted cholesterol in NT and *GRAMD1B* shRNA cells by culturing cells in lipoprotein-free FBS and in the presence of Simvastatin ($10 \mu\text{mol}/\text{L}$; Fig. 6A) and then assessed their invasiveness. *GRAMD1B* knockdown led to an increase in free cholesterol (Fig. 6A) and invasion (Fig. 6B), but cholesterol depletion abolished this increased invasiveness (Fig. 6B). Next, we sought out to determine how free cholesterol promotes melanoma cell invasion. Excess free cholesterol in cells can be metabolized into oxysterols to aid steroid and bile synthesis or esterified and stored in lipid droplets (61). Interestingly, the oxysterol 27-hydroxycholesterol (27-HC) has been implicated as a breast cancer metastasis driver (62–64). Consistent with this, we found that exogenous treatment of A375 and SKMEL2 cells with cholesterol and 27-HC was sufficient to stimulate invasiveness (Fig. 6C). To test if 27-HC could be a driver of the metastatic behavior in a *GRAMD1B* KO setting, we first assessed the expression of *CYP27A1*, the mitochondrial resident enzyme that synthesizes 27-HC from cholesterol in cells. Our RNA-seq results showed that *CYP27A1* is the only

oxysterol enzyme expressed in SKMEL2 cells and its expression was further increased upon *GRAMD1B* loss (Supplementary Fig. S8A). Real-time PCR and Western blot analysis confirmed a robust increase in *CYP27A1* mRNA (Supplementary Fig. S8B) and protein levels (Fig. 6D) upon *GRAMD1B* loss in SKMEL2 and A2058 cells. To directly test the role of *CYP27A1* in melanoma cell invasion, we knocked down *CYP27A1* in three human melanoma cell lines (Supplementary Fig. S8C; Fig. 6E) and assessed tumor cell invasion. We observed that *CYP27A1* knockdown by itself potently suppressed invasion (Fig. 6F). Next, to definitively test the contribution of 27-HC to the invasiveness of *GRAMD1B* KO cells, we knocked down *CYP27A1* in NT or *GRAMD1B* KO SKMEL2 cells (Fig. 6G and H). We observed that *CYP27A1* knockdown diminished the invasiveness of *GRAMD1B* KO cells (Fig. 6I), suggesting that 27-HC is a key mediator of the metastatic phenotype upon *GRAMD1B* loss.

Sterols can drive invasion through changes in metabolism and cell signaling (65, 66), membrane synthesis (67, 68), or transcriptional programs (63, 64, 69). Previous studies have shown that activation of melanoma invasiveness and metastasis is largely governed by transcriptional cell state changes (70–75), including those associated with AP-1 as a key transcription factor linked to invasive/migratory cell states in melanoma (76, 77). To further investigate this, we performed Hypergeometric

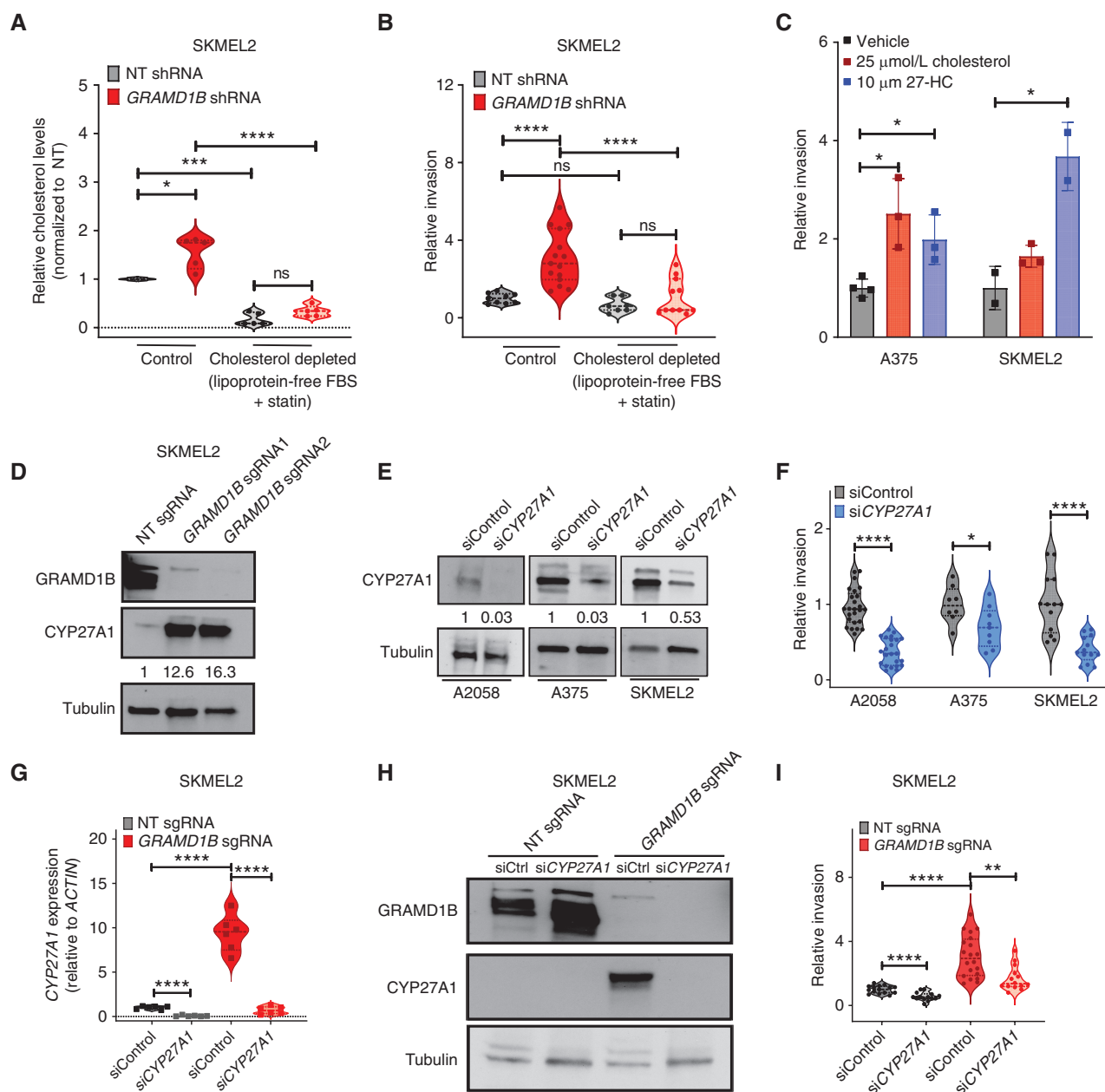


Figure 6. Free cholesterol and 27-hydroxycholesterol promote tumor invasion under GRAMD1B loss. **A**, Quantification of relative cholesterol levels (represented as fold change and normalized to NT cells) in SKMEL2 NT and GRAMD1B shRNA cells cultured in control media or cholesterol-depleted media. To deplete cholesterol, cells were grown in media containing 10% lipoprotein-free FBS and Simvastatin for 48 hours. See Methods for details. Data are pooled from $n = 3$ independent experiments; error bars, SD; Welch t test was used to assess statistical significance. *, $P = 0.018$; ***, $P = 0.0005$; ****, $P < 0.0001$. **B**, Quantification of relative invasion in cells from **A**. The number of fluorescent cells in the bottom chamber was quantified and normalized to the NT group to obtain relative invasion. Data are pooled from $n = 3$ independent experiments; error bars, SD; Welch t test was used to assess statistical significance. ****, $P = 0.0001$; *****, $P < 0.0001$. **C**, Quantification of relative invasion (represented as fold change and normalized to vehicle) in A375 and SKMEL2 cells treated with cholesterol (25 μmol/L) or 27-hydroxycholesterol (27-HC, 10 μmol/L) for 48 hours. The number of fluorescent cells in the bottom chamber was quantified and normalized to the vehicle group to obtain relative invasion. Data are pooled from $n = 3$ independent experiments; error bars, SD; Welch t test was used to assess statistical significance. *, $P < 0.05$. **D**, Western blot analysis of CYP27A1 and GRAMD1B in SKMEL2 NT and GRAMD1B KO cells. CYP27A1 levels normalized to Tubulin are in black text below the blot. **E**, Western blot analysis of CYP27A1 in A2058, A375, and SKMEL2 cells transfected with control siRNA or CYP27A1 siRNA. CYP27A1 levels normalized to Tubulin are in black text below the blot. **F**, Relative invasion of A2058, A375, and SKMEL2 cells transfected with control siRNA or CYP27A1 siRNA. The number of fluorescent cells in the bottom chamber was quantified and normalized to control cells to obtain relative invasion. Data are pooled from $n = 3$ independent experiments; error bars, SD; Welch t test was used to assess statistical significance. *, $P < 0.05$; ****, $P < 0.0001$. **G**, Real-time PCR analysis of CYP27A1 in SKMEL2 NT and GRAMD1B KO cells transfected with control siRNA or CYP27A1 siRNA. Data are pooled from $n = 3$ independent experiments; error bars, SD; Welch t test was used to assess statistical significance. ****, $P < 0.0001$. **H**, Western blot analysis of CYP27A1 and GRAMD1B in SKMEL2 nontargeting (NT) and GRAMD1B KO cells transfected with control siRNA or CYP27A1 siRNA. Data are pooled from $n = 3$ independent experiments; error bars, SD; Welch t test was used to assess statistical significance. ****, $P < 0.0001$; **, $P < 0.01$.

Optimization of Motif EnRichment (HOMER) analysis on GRAMD1B KO versus NT cells, in order to infer which transcription factors were driving changes in gene expression, as shown previously (70, 78, 79). This revealed that members of the AP-1 family—FOSL1, FOSL2, and JUNB—were among the topmost enriched motifs in the KO cells (Fig. 7A). FOSL1 belongs to the FOS family of proteins consisting of c-FOS, FOSL1, FOSL2, and FOSB (80). These encode leucine zipper proteins that dimerize with JUN proteins to form a stable AP-1 transcription factor complex (80). This led us to assess whether free sterol accumulation in KO cells activates AP-1. To test this, we first asked if cholesterol or 27-HC was sufficient to activate AP-1 using an AP-1 luciferase reporter assay. Treatment of human melanoma A375 and SKMEL2 cells with cholesterol or 27-HC potently activated the AP-1 reporter (Fig. 7B and C) but failed to activate a control luciferase reporter (Supplementary Fig. S8D and S8E). Importantly, *GRAMD1B* depletion also led to potent activation of AP-1 reporter (Fig. 7D) without affecting the control construct (Supplementary Fig. S8F).

The AP-1 Complex Drives Melanoma Cell Invasion through ERK

The AP-1 complex and its subunits are regulated in response to growth factors, cytokines, and cell stress in mammalian cells (80). For example, cellular stress can activate the p38 or JNK pathway to regulate *JUN* transcription and AP-1 activation. Growth factor signaling, on the other hand, can activate ERK signaling to promote *FOS* transcription as well as phosphorylate the AP-1 complex to its active form (80). To better understand how AP-1 is activated under *GRAMD1B* depletion, we treated NT and *GRAMD1B* shRNA cells with chemical inhibitors of the JNK and ERK pathways (Supplementary Fig. S8G) and performed the AP-1 luciferase assay. *GRAMD1B* knockdown enhanced AP-1 activation as expected (Fig. 7E). Although the JNKi suppressed AP-1 activity in the NT cells, it failed to rescue AP-1 activation in *GRAMD1B* knockdown cells. In contrast, the ERKi led to a decrease in AP-1 activation in the knockdown cells (Fig. 7E). These data suggest that ERK signaling may be driving AP-1 activation in *GRAMD1B* KO cells. Indeed, loss of *GRAMD1B* led to potent phosphorylation of ERK1/2 in three independent melanoma cell lines (Fig. 7F). Additionally, real-time PCR analysis revealed that *JUN*, *FOSL1*, and *FOSL2* transcripts were upregulated upon *GRAMD1B* loss in SKMEL2 cells (Supplementary Fig. S8H), further implicating the ERK pathway in AP-1 activation. Exogenous cholesterol and 27-HC also induced ERK activation (Fig. 7G; Supplementary Fig. S8I), but which of these was more potent differed across cell lines. In A375 and A2058, 27-HC was sufficient to increase pERK, whereas in SKMEL2, cholesterol itself was more effective in inducing pERK. We speculate this cell line specificity may be due to differences in uptake, as we found that the addition of cholesterol complexed with methyl cyclodextrin failed to induce pERK in A375 cells (Fig. 7G), but LDL cholesterol potently activated pERK in these cells (Supplementary Fig. S8I). Finally, to test the contribution of activated ERK signaling to the enhanced invasiveness in the KO cells, we treated NT and *GRAMD1B* knockdown SKMEL2 cells with a low dose (100 nmol/L) of ERKi for 24 hours and performed a transwell invasion assay. Treatment of *GRAMD1B* knockdown cells with the

ERKi suppressed invasion without affecting cell proliferation (Fig. 7H; Supplementary Fig. S8J). Taken together, our data demonstrate that free sterols in *GRAMD1B* KO cells activate ERK signaling to promote an AP-1-mediated invasion program and metastasis in melanoma cells (Fig. 7I).

DISCUSSION

The incidence of localized melanoma far exceeds that of metastatic disease. Discerning which lesions will go on to metastasize is of urgent clinical need, both to avoid overtreatment of lesions with a benign course and to provide adjuvant therapy to those with a more aggressive course. Although clinical, histologic, imaging, and transcriptional signatures have all been used to make such predictions (18–28, 81–84), these do not provide mechanistic insight into how those signatures act to promote metastasis. Mouse models of melanoma to study these mechanisms are powerful but can be limited in their scalability for genetic perturbation (30, 32, 33). For this reason, we developed a zebrafish TEAZ-based metastasis platform as a rapid and scalable system for studying these human gene signatures. Through our screen, we identified *GRAMD1B*, a cholesterol transfer protein, as a novel metastasis suppressor in melanoma. Our work sheds light on an understudied protein in cancer and identifies a new role for interorganelle cholesterol trafficking in melanoma metastasis.

The cholesterol carrier APOE has been previously linked to metastasis in melanoma (85–88). Studies into the use of statins prior to melanoma diagnosis have shown it may reduce risk of melanoma recurrence (89), although the mechanism is not clear. Additionally, cholesterol homeostasis is a metabolic dependency in other tumor types (63, 67, 90, 91). Cholesterol in mammalian cells is obtained either from receptor-mediated uptake or from *de novo* cholesterol synthesis in the ER (61). Sixty percent to 80% of cellular cholesterol is transported and stored in the PM, where it is critical to maintain membrane structural integrity (61). It is also transported to the ER, where it is esterified and stored as lipid droplets and suppresses SREBP2-mediated *de novo* cholesterol synthesis, thus maintaining homeostasis (58, 61, 92). However, how organelles transfer cholesterol among each other and how this functions in cancer is not completely understood.

GRAMD1B represents a recently characterized cholesterol transfer protein, with a GRAM domain that recognizes unesterified accessible cholesterol and a StART-like domain that transfers cholesterol through membrane contact sites (MCS; ref. 48). A recent study identified that *GRAMD1B* may also transport carotenoids within retinal cells (93), necessitating a need to better understand its role in mammalian cells. *GRAMD1B* was shown to reside in the ER but upon cholesterol loading (complexed with methyl cyclodextrin or HDL cholesterol) forms MCS with the PM to transfer accessible cholesterol pools from the PM to the ER (46, 48, 56). There are conflicting data as to the consequences of *GRAMD1B* loss. Previous work showed that *GRAMD1B* loss leads to a block in PM to ER cholesterol transport, reduced cholesterol esterification in the ER, and activation of the SREBP2 pathway, which may be in part dependent upon phosphatidylserine in the inner leaflet of the PM (46, 48, 55). However, Höglinger and colleagues showed that *GRAMD1B* depletion in HeLa cells led

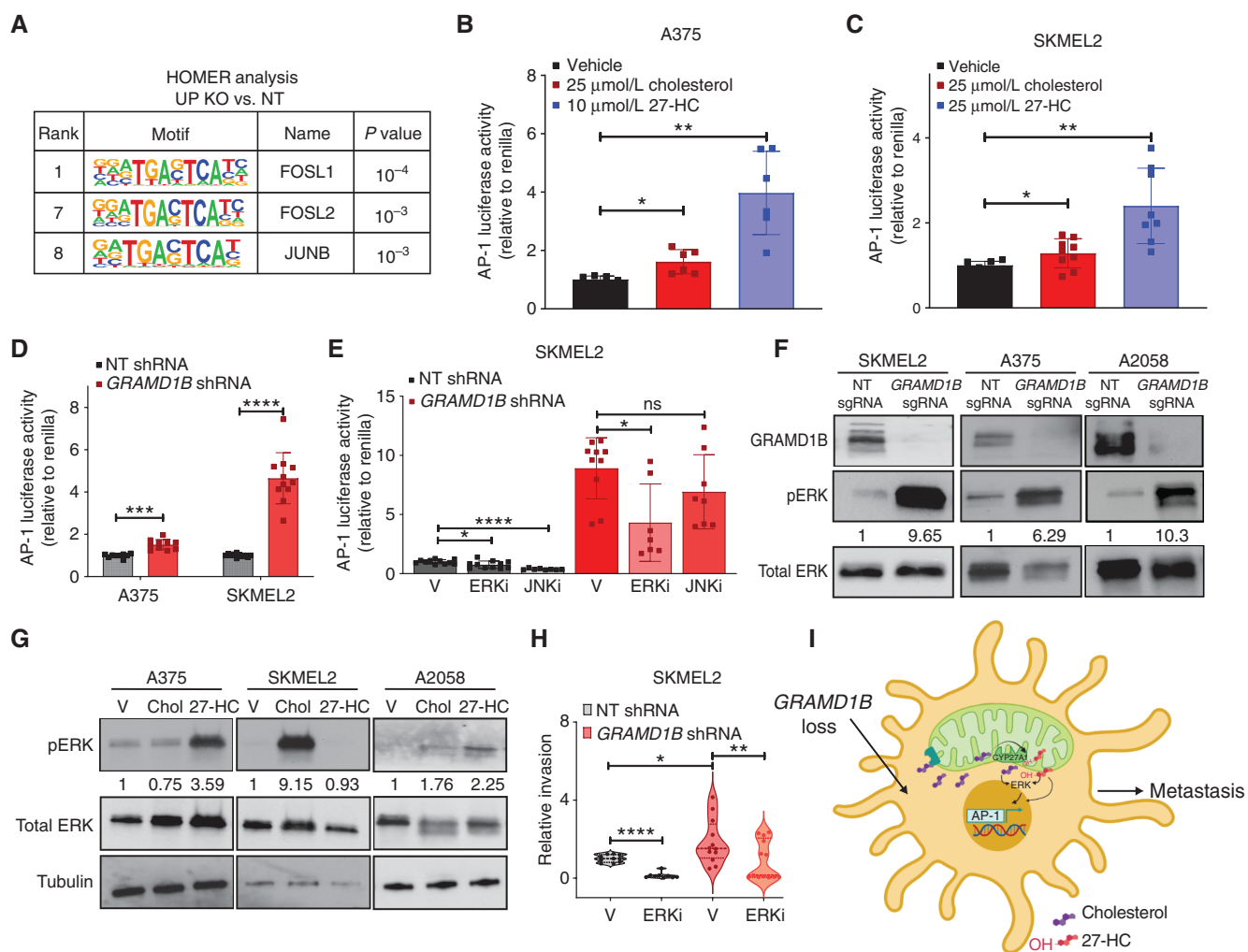


Figure 7. Sterol overload activates AP-1 via ERK signaling to mediate invasion upon GRAMD1B loss in melanoma. **A**, HOMER analysis of top motifs enriched in genes upregulated in GRAMD1B KO cells. Motifs related to the AP-1 complex are highlighted in the table along with rank and P value. Dual reporter analysis of AP-1 luciferase reporter activity in A375 cells treated with 25 μmol/L cholesterol or 10 μmol/L 27-HC for 48 hours. Firefly AP-1 luciferase activity was normalized to Renilla luciferase and relative luciferase activity is plot normalized to vehicle. Data are pooled from $n = 3$ independent experiments. Error bars, SD; Welch t test was performed to assess statistical significance. *, $P = 0.01$; **, $P = 0.001$. **B**, Dual reporter analysis of AP-1 luciferase reporter activity in SKMEL2 cells treated with 25 μmol/L cholesterol or 25 μmol/L 27-HC for 48 hours. Firefly AP-1 luciferase activity was normalized to Renilla luciferase and relative luciferase activity is plot normalized to vehicle. Data are pooled from $n = 3$ independent experiments. Error bars, SD; Welch t test was performed to assess statistical significance. *, $P = 0.04$; **, $P = 0.002$. **D**, Dual reporter analysis of AP-1 luciferase reporter activity in A375 and SKMEL2 nontargeting (NT) or GRAMD1B knockdown cells. Firefly AP-1 luciferase activity was normalized to Renilla luciferase and relative luciferase activity is plot normalized to NT shRNA. Data are pooled from $n = 3$ independent experiments. Error bars, SD; Welch t test was performed to assess statistical significance. ***, $P = 0.0003$; ****, $P = 0.000038$. **E**, Dual reporter analysis of AP-1 luciferase reporter activity in SKMEL2 NT or GRAMD1B knockdown cells treated with DMSO (vehicle), 200 nmol/L JNKi or 200 nmol/L ERKi for 48 hours. Firefly AP-1 luciferase activity was normalized to Renilla luciferase and relative luciferase activity is plot normalized to NT shRNA (vehicle). Data are pooled from $n = 3$ independent experiments. Error bars, SD; Welch t test was performed to assess statistical significance. *, $P = 0.01$; ****, $P < 0.000001$. V, vehicle. **F**, Western blots depicting phosphorylation of ERK1/2 in SKMEL2, A375, and A2058 cells expressing NT or GRAMD1B sgRNAs. Data are representative of $n = 2-3$ independent experiments. Quantification of phosphorylated ERK protein levels relative to total ERK in black text below the blot. **G**, Western blots depicting phosphorylation of ERK1/2 in A375, SKMEL2, and A2058 cells stimulated with cholesterol or 27-HC for 48 hours. Data are representative of $n = 2$ independent experiments. Quantification of phosphorylated ERK protein levels relative to total ERK in black text below the blot. **H**, Quantification of relative invasion in SKMEL2 cells expressing NT or GRAMD1B shRNA treated with 100 nmol/L ERKi for 24 hours. The number of Hoechst+ cells in the bottom chamber in each group was normalized to the NT group to obtain relative invasion. See Methods for details. Data are pooled from $n = 3$ independent experiments. Error bars, SD; Welch t test was performed. *, $P < 0.05$; **, $P < 0.01$; ****, $P < 0.0001$. **I**, Working model of prometastatic functions of GRAMD1B loss in melanoma. GRAMD1B loss results in free cholesterol, some of which may move into the mitochondria, where it is converted to 27-HC. Free sterols induce ERK signaling to activate the AP-1 complex and mediate an invasion transcriptional program in melanoma to promote metastasis.

to an increase in free cholesterol (57). Our data also report an increase in free cholesterol within cells upon GRAMD1B loss, without any significant alteration to levels of choline-containing phospholipids or membrane fluidity. The mechanisms of free cholesterol accumulation and transport upon GRAMD1B

loss in melanoma require further exploration. Höglinger and colleagues also observed increased lysosome-mitochondria MCS in GRAMD1B knockdown cells, indicating that under GRAMD1B depletion, free cholesterol may move into the mitochondria instead of the ER (57). Another study observed an

increase in mitochondrial cholesterol upon loss of GRAMD1C in renal cancer cells (94). These findings along with ours raise the intriguing possibility that GRAMD1B loss in melanoma leads to a relative increase in mitochondrial cholesterol. Once in the mitochondria, cholesterol can be converted into 27-HC through the action of CYP27A1 (sterol 27-hydroxylase enzyme; refs. 95, 96) and promote metastasis.

There is growing evidence that 27-HC, the stoichiometric downstream metabolite of cholesterol, can promote tumorigenesis of breast cancer stem cells (97) and metastasis of breast cancer cells through tumor-intrinsic mechanisms as well as recruitment of immune cells (62–64, 98, 99). Consistent with these findings, we observe that both cholesterol and 27-HC stimulate the invasiveness of melanoma cells. Importantly, we show that 27-HC is a key mediator of the effects of GRAMD1B loss on tumor cell invasion. The accumulated free sterols in turn activate an AP-1 tumor invasion program through potent ERK signaling to promote metastasis. This finding is of significance because AP-1 is linked to migratory and invasive states in melanoma (76, 77). Interestingly, 27-HC has also been reported to function as an endogenous selective estrogen receptor modulator (SERM; refs. 69, 100). Ligand-activated estrogen receptors can be recruited to AP-1 sites to promote gene transcription (101, 102). Whether 27-HC functions as a SERM in melanoma and plays a role in activating an ER/AP-1 invasion program needs to be explored. Potent ERK signaling in GRAMD1B KO cells potentiates AP-1 activity, at least partly by transcriptionally upregulating the AP-1 members *JUN*, *FOSL1*, and *FOSL2*. How free sterols activate ERK in melanoma cells requires future exploration. Our findings show that exogenous cholesterol and 27-HC can activate ERK signaling in A375 and A2058 melanoma cells, but only cholesterol itself activated pERK in SKMEL2 cells. Whether this is due to differences in uptake mechanisms versus intracellular processing to 27-HC is an important area for future exploration. It is also possible that free sterols promote tumor cell invasion through additional non-ERK mechanisms (Fig. 7I). These findings further highlight a need to study the consequences of cholesterol delivery and transport within cells on subsequent prometastatic cell signaling.

A recent study showed that *GRAMD1B* knockdown promotes breast cancer migration via activation of JAK–STAT signaling (103). Consistent with this, our transcriptomics data also revealed activation of the JAK–STAT pathway in GRAMD1B KO cells, suggesting additional mechanisms may be at play in the KO cells (Fig. 4D). Indeed, inflammatory signaling such as JAK–STAT and NF- κ B pathways have been implicated in driving metastasis (104–107). The activation of inflammatory transcriptional signatures observed in GRAMD1B KO cells (Fig. 4D) highlights a need to additionally explore the contribution of the immune compartment to the metastasis observed *in vivo*. Our data indicate that the AP-1 tumor invasion transcriptional program represents at least one mechanism by which GRAMD1B loss promotes metastasis.

Given the large caseload of localized melanoma, our work highlights the importance of identifying which lesions will go on to metastasize and how those high-risk lesions can be therapeutically targeted. Recent work using adjuvant BRAF/MEKi or PD-1/PD-L1 therapies has shown substantial reductions in subsequent metastatic relapse and mortality (14–16, 108). Our data suggest that dysregulated cholesterol

trafficking inside cells may be an additional important target and that mechanisms to modulate the synthesis of 27-HC may be one way of preventing relapse of high-risk disease.

METHODS

Plasmids

An sgRNA plasmid (MITF GFP 2X-sgRNA), which harbors a *mitfa*:GFP insert as well as a 2X sgRNA cassette (Fig. 2A), was generated for the zebrafish screen. The 2X sgRNA cassette from MAZERATI 2X (MAS2X) sgRNA (RRID Addgene_118844), also called MiniCoopR 2X sgRNA (gift from Dr. Len Zon), was amplified and introduced into *mitfa*:GFP plasmid using In-fusion cloning. Site-directed mutagenesis was performed to introduce NheI sites spanning sgRNA2 of the plasmid. MAS2X *sgpten* was cloned from MAS2X sgRNA (Supplementary Fig. S2A; ref. 44, 109). The U6-sgRNA plasmid (RRID Addgene_64245) was used along with *mitfa*:Cas9 plasmid and MiniCoopR:tdTomato (previously developed in the lab). LentiCRISPRV2 Puro (RRID Addgene_52961), psPAX2 (RRID Addgene_12260), and MD2 (RRID Addgene_12259) plasmids were obtained from Addgene. TRIPZ shRNA plasmids were purchased from Dharmacon expressing a non-targeting (NT) shRNA or shRNAs against human GRAMD1B. Clone IDs and hairpin sequences are in Supplementary Table S3. Control luciferase plasmid (pGL3, RRID Addgene_48743) and Renilla luciferase plasmid (pRL-SV40, RRID Addgene_27163) were obtained from Promega (E1751 and E2231) and pGL3-AP-1 was from Addgene (RRID Addgene_40342). Details of the oligonucleotide sequences used for cloning and sequencing are in Supplementary Table S3.

Cell Culture

A375 (RRID:CVCL_A2CR), A2058 (RRID:CVCL_1059), and SKMEL2 (RRID:CVCL_0069) cells were obtained in August 2013 from the ATCC, which performs cell line authentication testing using morphology, karyotyping, and PCR-based methods including short-tandem repeat profiling to confirm the identity of human cell lines. The cells were also tested for *Mycoplasma* using a luminescence-based assay (Mycoalert Mycoplasma Detection Kit, Lonza) in 2017. SKMEL5 (RRID:CVCL_0527) cells were obtained in 2021 from ATCC. Cells were cultured in DMEM High Glucose media (Invitrogen) supplemented with 5% FBS (Sigma-Aldrich) and 1% antibiotics, 1% glutamine (Invitrogen). ZMEL-LD cells were established previously in the lab (110) and a low passage culture was utilized for gene editing experiments. For exogenous sterol treatment assays, melanoma cells were treated with 25 μ mol/L cholesterol (Sigma) or 10–25 μ mol/L 27-HC (Sigma) for 48 hours. For chemical inhibitor experiments, melanoma cells were treated with 100 nmol/L–200 nmol/L of SCH772984 (ERKi) and JNK-IN-8 (JNKi) for 24 hours (invasion assays) or 48 hours (luciferase assays). A list of all chemicals, kits, and their source is available in Supplementary Table S4.

Zebrafish Husbandry

Zebrafish experiments were carried out in accordance with institutional animal protocols. Animals were housed in a temperature-(28.5°C) and light-controlled (14 hours on, 10 hours off) facility. Fish were fed thrice a day using brine shrimp and pelleted zebrafish food. All anesthesia was done using tricaine (Western Chemical Incorporated) with a stock of 4 g/L (protected for light) and diluted until the fish was immobilized. All procedures were approved by and adhered to Institutional Animal Care and Use Committee (IACUC) protocol #12-05-008 through Memorial Sloan Kettering Cancer Center. Fish strains used in this study are in Supplementary Table S4.

TEAZ Metastasis Screening

AVAST-M Melanoma Cohort and Gene Expression Data Generation. Data on differentially expressed human genes were extracted from

the phase III adjuvant AVAST-M study (17, 37). The study (including the collection of DNA and RNA) was ethically approved in accordance with the Declaration of Helsinki (REC reference number 07/Q1606/15, March 16, 2007). Participants provided written informed consent to sampling of their tumor blocks during study recruitment. Extracted RNA was sequenced and aligned as previously described (23). RNA-seq data were available on 204 primary melanoma samples, of which 10 samples were removed from downstream analyses owing to a lack of data on all clinical covariates, resulting in a final $n = 194$ samples. Data were also available on 175 regional lymph node samples, of which 32 samples were removed from the downstream analyses owing to a lack of data on all clinical covariates, resulting in a final $n = 143$ samples.

DE Analyses. DE analyses between early-stage melanoma tumors that became metastatic versus those that remained nonmetastatic over the 6-year study period were performed using the package DESeq2 (111; v1.18; R v3.6.1). The negative binomial models were considered controlled for the clinical covariates stage, Breslow thickness, Eastern Cooperative Oncology Group Performance Status, and treatment, as well as for the library size (offset), full details are available in Garg and colleagues (23). In contrast to the DE analysis used to generate the signature described by Garg and colleagues, in this analysis, only the metastasis suppressor genes, whereby reduced expression within the primary tumor was associated with patients with metastases, were considered. Additionally, the covariate corrected DE was undertaken separately on primary melanomas ($n = 194$) and regional lymph node tumors ($n = 143$) and only the intersecting genes (downregulated in both datasets) were selected for further testing and are summarized in Supplementary Table S1. These ($n = 41$) genes include *CCR5*, *PLA2G2D*, *TNFRSF10A*, *KIF19*, *GBP5*, *FASLG*, *SOC31*, *TAS2R60*, *SLIT1*, *CLIC5*, *AIM2*, *PIK3R6*, *GRAMD1B*, *LAG3*, *UTS2*, *GLDC*, *GCH1*, *PRF1*, *ARRDC1*, *SMTNLI*, *TRABD2A*, *MFSD6L*, *RGS7*, *SFMBT2*, *KYNU*, and *TRIM22*.

In contrast to the study by Garg and colleagues, an additional series of DE analyses were undertaken to generate a further list of genes associated with brain metastases, identified as an important area of unmet need. Only the metastasis suppressor genes, whereby reduced expression within the primary tumor associated with patients with brain metastases, were considered. Second, as opposed to the two phenotypes considered in the “pan-organ” metastases analysis, we considered 3 different brain metastasis phenotypes resulting in 3 DE analyses: (i) brain versus extracranial metastases, (ii) brain-only metastases (defined as metastases to the brain at the first presentation of metastatic disease in the absence of any extracranial disease sites) versus extracranial metastases, and (iii) brain-only metastases versus no distant metastases. Each of these analyses was undertaken separately on the primary melanoma and regional lymph node datasets. To be considered for functional testing, a gene needed to be significantly downregulated in only one of three brain metastasis DE analyses, but significantly downregulated in both the primary melanoma and lymph node datasets.

Analysis of AVAST-M Genes in cBioPortal. The TCGA Melanoma Firehose Legacy ($n = 287$ samples), Metastatic Melanoma UCLA 2016 dataset ($n = 38$ samples), and other available subcutaneous melanoma datasets were analyzed in cBioPortal (40) to generate an OncoPrint of AVAST-M gene alterations in these datasets.

Pathway Analysis of AVAST-M Genes. The 61 genes from the AVAST-M signature were subject to PANTHER analysis using <http://www.pantherdb.org/> (112, 113).

sgRNA Design for the Screen. Zebrafish orthologs for genes from the metastasis signature were retrieved from ZFIN (45), University of Oregon, Eugene, OR 97403-5274; <http://zfin.org/>, and CRISPOR

(114) tool was used to design 4 sgRNAs against each target gene. For the pilot screen, 9 of 61 genes were chosen. The sgRNAs (Supplementary Table S3) were consecutively cloned into MG2X using AarI sites and then the NheI site-based restriction digestion. Additionally, sgRNAs against *ptena* and *ptenb* were cloned into a U6-sgRNA plasmid (Supplementary Table S3).

TEAZ Screen. TEAZ was utilized to generate melanomas as previously described (36). To develop a baseline model of metastasis, *casper mitfa:BRAF^{V600E} tp53^{-/-}* transgenic animals (4–5 months old) were electroporated with MAS2X *sgpten* (500 ng), *mitfa:GFP* (112 ng) and Tol2 (66 ng) plasmids to generate *BRAF^{V600E}, tp53^{-/-}, pten^{-/-}* tumors. For the metastasis screen, plasmids electroporated per fish included U6-*ptena* (40 ng), U6-*ptenb* (40 ng), and Mini-CoopR-tdTomato (320 ng) to induce melanocyte rescue, MG2X-sgRNA_12, MG2X-sgRNA_34 (100 ng each), and Tol2 (88 ng) and *mitfa:Cas9* (200 ng). Briefly, adult male fish were anesthetized with 0.2% tricaine and injected with 1 μ L of the plasmid mix described above into the skin below the dorsal fin. Fish were electroporated and allowed to recover in freshwater. Electroporation was performed using CM830 Electro Square Porator from BTX Harvard Apparatus and Genepaddles 3×5 mm, with a voltage of 45 V, 5 pulses, 60 ms pulse length and 1 s pulse interval. Fish were imaged every week using brightfield and fluorescent imaging at 25 \times and 10 \times using a Zeiss Axio microscope. Primary tumor growth was measured at 4 and 8 weeks and quantified using ImageJ. Metastasis was monitored in the kidney marrow via fluorescent imaging at 10 \times at 12 weeks after TEAZ, in areas separate from the primary tumor as previously described (115). Manual scoring was performed based on fluorescent images to obtain metastatic incidence. Metastatic burden was calculated by quantifying the Corrected Total Cell Fluorescence in the kidney marrows of animals at 12 weeks after TEAZ after background correction.

Histology. Tumor-bearing zebrafish were euthanized in 0.2% tricaine and fixed in 4% PFA for 72 hours. Animals were transferred to 70% ethanol and subjected to sagittal sectioning to capture the head, kidney marrow, and primary tumor on a slide. Histology was performed by HistoWiz Inc. (histowiz.com) using a Standard Operating Procedure and fully automated workflow. Samples were processed, embedded in paraffin, and sectioned at 5 μ m. IHC was performed on a Bond Rx autostainer (Leica Biosystems) with enzyme treatment (1:1,000) using standard protocols. Antibodies used were rat monoclonal F4/80 primary antibody (eBioscience, 14-4801, 1:200) and rabbit anti-rat secondary (Vector, 1:100). H&E staining was performed to histologically confirm melanomas. Sections were stained with a BRAFV600E antibody (ab228461, RRID AB_2833072), phospho-AKT antibody (CST4060, RRID AB_2315049), and antibodies against GFP (ab183734, RRID AB_2732027), and RFP (#600-401-379, RRID AB_2209751) to confirm the genotypes of melanomas and stain tumor cells. Animals with tumors expressing NT and *gramd1b* sgRNAs were sectioned and stained with RFP to visualize metastatic tumor cells in the kidney marrow. Histology of mouse tissues was similarly performed; H&E staining was used to histologically assess the presence of metastasis in liver and lung tissues. Bond Polymer Refine Detection (Leica Biosystems) was used according to the manufacturer’s protocol. After staining, sections were dehydrated and film coverslipped using a TissueTek-Prisma and Coverslipper (Sakura). Whole slide scanning (40 \times) was performed on an Aperio AT2 (Leica Biosystems). Antibodies and concentrations used are listed in Supplementary Table S4.

CRISPR Sequencing and Surveyor Assays. Primers were designed to amplify an amplicon of 200 to 280 bp in length where the mutation site targeted by sgRNA is within 100 bp of the beginning or end of the amplicon (Supplementary Table S3). Fish of interest were euthanized and dissected carefully under microscopy to isolate as much

of the tumor as possible, 7 to 8 weeks after TEAZ. Tail tissue of fish was used as a negative control. Genomic DNA was isolated from tumor samples using the Qiagen DNeasy Blood and tissue kit. Promega GoTaq Green master mix was used to amplify the amplicon of interest. PCR products were visualized on a DNA gel and purified to submit samples for CRISPR sequencing. CRISPR sequencing results were analyzed using CRISPR Variants R package (116) to obtain gene editing frequency in tumor samples. For surveyor assays, genomic DNA was subject to the surveyor nuclease assay (IDT). Gene editing was confirmed on a 2% agarose DNA gel.

Generation of KO Cells Using CRISPR-Cas9

HEK 293T (1×10^8) cells cultured in 10-cm dishes were cotransfected with lentiCRISPR V2 (1.5 μ g), psPAX2 (0.6 μ g), and pMD2.g (0.3 μ g) helper plasmids using Qiagen Effectene reagent as per manual instructions. Lentiviral supernatant was collected 72 hours after transfection and filtered. Recipient cells were infected overnight with viral supernatant containing 10 μ g/mL polybrene (Sigma-Aldrich) and replenished the next day with fresh media. After 48 hours, transduced cells were cultured in fresh media containing 1 μ g/mL puromycin for 7 days and then utilized for experiments.

Generation of GRAMD1B shRNA Cells

HEK 293T (1×10^8) cells cultured in 10-cm dishes were cotransfected with psPAX2 (0.6 μ g), pMD2.g (0.3 μ g) helper plasmids along with Dharmacon's pTRIPZ dox-inducible shRNA plasmids or Sigma's pLKO shRNA plasmids (2 μ g) using Qiagen Effectene reagent as per manual instructions. Lentiviral supernatant was collected 72 hours after transfection and filtered. Recipient cells were infected overnight with viral supernatant containing 10 μ g/mL polybrene (Sigma-Aldrich) and replenished the next day with fresh media. After 48 hours, transduced cells were cultured in fresh media containing 1 μ g/mL puromycin for 7 days and then utilized for experiments. The dox-inducible shRNA cells were pretreated with 4 μ g/mL dox for 72 hours for most experiments.

RNA Extraction and Quantitative Real-time PCR Analysis

Total RNA was extracted from cells, and 1 to 2 μ g of RNA was subjected to cDNA synthesis using the Invitrogen SuperScript First-Strand Synthesis Kit. Real-time PCR analysis was performed on cDNA using a 2X PowerSybr master mix. mRNA levels were normalized to *ACTIN*, with gene expression levels measured using a standard curve for each set of primers crossing exon–exon junctions. Real-time PCR primers are listed in Supplementary Table S3.

RNA-seq of SKMEL2 Cells

SKMEL2 NT or GRAMD1B KO cells were cultured in 10-cm dishes and harvested for RNA isolation in triplicates ($n = 3$ per group) and used for cDNA synthesis and barcoding with Illumina adapters, followed by sequencing on Illumina NovaSeq 6000. RNA-seq reads in fastq format were quantified by Salmon (117) to a prebuilt index of the hg38 human transcriptome from Ensembl accounting for GC biases. Resulting count matrices were used as input for DESeq2 (111) in R for normalization and DE analysis using the default parameters. Normalized counts were used as input for GSEA (118, 119). Heat maps were generated using the R package complexheatmap, and waterfall plot was generated using the R package mvhsplots (<https://github.com/mvhunter1/mvhsplots>). Homer analysis was performed based on a previously established protocol (78) on genes upregulated in GRAMD1B KO cells.

Survival Analyses

The bulk RNA-sequencing gene expression data from the AVAST-M cohort were normalized using variance stabilizing transformation. *GRAMD1B* gene expression signature was obtained by standardizing

GRAMD1B gene expression in all the samples to have zero mean and unit variance. This standardized *GRAMD1B* expression signature was used as a continuous predictor in Cox regression models fitted by means of the `coxph` function of the survival package (v3.2-7) in R (v4.0.3). Samples were divided into groups based on median (standardized) *GRAMD1B* expression values for plotting Kaplan–Meier survival curves. Here, samples having higher than or equal to median expression values were grouped as “high,” otherwise grouped as “low.” The Kaplan–Meier plots were made using the `survminer` package (v0.4.8).

The independent replication of the survival was conducted using data from the Leeds Melanoma Cohort [European Genome-phenome Archive (EGA) under accession number EGAS00001002922; ref. 24]. This is a population-ascertained cohort study consisting exclusively of primary melanomas (stages I–III) coupled with long-term clinical follow-up. mRNA extracted formalin-fixed, paraffin-embedded tissue-derived primary tumors ($n = 687$ samples) were analyzed on the Illumina DASL-array platform. The survival time was calculated from the time of diagnosis to the time of last follow-up or time of death from melanoma, whichever occurred first and referred to as melanoma-specific survival. The final sample size was $n = 666$ after removing patients who died of other causes than melanoma. In order to provide optimal group balance for the visual representation of the survival curves, the analysis was stratified on Breslow thickness <3 mm or >3 mm. In order to better reflect samples from the AVAST-M study (late-stage tumor stage IIB–IIIC), the analysis was stratified on Breslow thickness <3 mm or >3 mm. The survival analysis was also considered for all \geq stage IIB tumors, regardless of Breslow thickness. *GRAMD1B* expression was dichotomized using the median value. These analyses were conducted in STATA v16.

Western Blotting

Cells and tissues were lysed in RIPA buffer (Invitrogen) containing Halt Protease Inhibitor Cocktail (Invitrogen) and homogenized via sonication. Proteins were quantified using the Bicinchoninic Acid Assay (Invitrogen), subject to separation using Biorad protein gradient gels, and transferred to a nitrocellulose membrane. The membranes were blocked for 1 hour at room temperature in 5% milk and probed with primary antibodies in 5% milk overnight at 4°C. After incubating the membrane with the appropriate secondary antibody conjugated to horseradish peroxidase for 1 hour at room temperature, protein levels were detected with SuperSignal Dura Extended Duration substrate (Thermo Fisher Scientific). Antibodies and concentrations used are listed in Supplementary Table S4.

Invasion and Migration Assays

SKMEL2 NT and GRAMD1B KO cells were seeded into a 0.5 \times BME-coated 96-well invasion chamber overnight as per (R&D Systems, 3455-096-K) manual instructions. The next day, invasion was measured, and data were normalized to invasion in the control group to obtain relative invasion. Because this kit was discontinued, invasion assays in Figs. 6 and 7 were performed using a Matrigel assay system (Corning Biocoat) in a 6-well format. Briefly, 250,000 cells (A375) or 500,000 cells (SKMEL2) were seeded onto Matrigel-coated invasion chambers as per the manual. The next day, Hoechst dye (1:2000) was added to the bottom chamber to stain nuclei of invaded cells. Hoechst⁺ invaded cells were imaged using a Zeiss fluorescent microscope with at least 4 to 6 fields per well, and ImageJ was used to quantify the number of invaded cells. Relative invasion was calculated by normalizing all data to the number of invaded cells in the control group. For the ERKi invasion experiments, Hoechst⁺ cells in the upper chamber were also quantified. Relative proliferation was calculated by normalizing Hoechst⁺ cell numbers normalized to the NT group 24 hours after drug treatment. For migration assays, 80,000 cells were seeded per insert into Corning's transwell cell-culture inserts (CLS3422) in serum-free media. Cell migration to the bottom chamber containing complete media was assessed by quantifying Hoechst⁺ cells as described above.

Tail-Vein Metastasis Assay

Animals were cared for in accordance with guidelines approved by the Memorial Sloan Kettering Cancer Center IACUC and Research Animal Resource Center. 200,000 dox-inducible SKMEL2 NT and *GRAMD1B* shRNA cells were injected into the tail veins of 5- to 6-week-old *NOD.Cg-Prkdcscid Il2rgtm1Wjl/SzJ* female mice (10 mice per group). Mice were kept on dox food for the duration of the experiment and weights and clinical signs were assessed daily. Three weeks after cell injection mice were euthanized, and gross necropsies were performed to assess metastasis. Livers, lungs, kidneys, and ovaries were collected from all mice and fixed in 4% PFA. Representative images of the organs were taken via Zeiss Axios microscopy at 6× magnification. Tissues were then submitted to Histowiz for histologic characterization.

H and E Metastasis Quantification

H&E sections from representative mice ($n = 2$ per experimental group) were subject to color deconvolution using the Qupath software H&E Brightfield setting. Sections were then thresholded to calculate tumor-positive area within 4 to 5 regions of interest of each liver lobe. Metastatic burden was calculated as % tumor-positive liver area.

Cell Proliferation Assays

One thousand SKMEL2 NT or *GRAMD1B* shRNA cells were pretreated with 4 $\mu\text{g}/\text{mL}$ dox for 48 h and then seeded in 96-well plates in 4 $\mu\text{g}/\text{mL}$ dox. Cell proliferation was measured over time using the Cyquant Direct cell proliferation kit as per manual instructions.

Immunofluorescence

SKMEL2 NT and *GRAMD1B* shRNA cells were pretreated with 4 $\mu\text{g}/\text{mL}$ dox for 3 days and seeded in 4-well chamber dishes (100,000 cells per well) in dox media overnight. The next day, cells were stained with Filipin according to Abcam's Cholesterol Cell-Based assay kit. Briefly, cells were fixed, and Filipin was added at 1:100 dilution in the staining buffer along with 1:100 Tubulin-Alexa488 (RRID AB_1502303) as a cytoplasmic marker, and chambers were incubated for 2h at room temperature. Chambers were washed thrice in PBS, mounted using Vectashield, and imaged on a confocal microscope (LSM880) using Airyscan, capturing at least 4 images at 60× for each group. Images were analyzed in ImageJ to quantify Filipin intensity within cells and the mean pixel value of Filipin signal in each group was calculated to depict intracellular cholesterol levels.

Cholesterol Extraction and Measurement in Cells

SKMEL2 NT or *GRAMD1B* shRNA cells (5×10^6 – 10×10^6) were trypsinized, counted, and centrifuged to obtain cell pellets for cholesterol extraction. Half of the cells were saved for protein extraction and quantification. The remaining half of the cells were washed 1× in PBS and then extracted with 200 μL of chloroform:isopropanol:NP-40 (7:11:0.1). Extracts were sonicated at an amplitude of 10%, with 10 total pulses of 1 second. Extracts were centrifuged for 10 minutes at 15,000 $\times g$, and the organic phase was transferred to a new tube. Tubes were air dried at 55°C to remove chloroform. The samples were then dried in a speed-vac to remove the remaining organic solvent for 20 minutes. Dried lipids were resuspended with 200 μL of Cholesterol Assay Buffer by vortexing until homogeneous. A standard curve was generated using Cholesterol standards in the kit. Cholesterol levels were quantified using the fluorescent Abcam cholesterol/cholesteryl kit as per manual instructions. For experiments in Fig. 5H and I and Fig. 6A, we used Promega's cholesterol/cholesterol ester glo assay kit (J3190) as this was more convenient in a 96-well format and amenable to high-throughput analysis of intracellular cholesterol. For these experiments, 8,000 NT or KO cells were seeded in a 96-well plate with at least 6 wells per condition. The next day, 3 wells per condition

were used to measure cholesterol as per the manual instructions. The remaining 3 wells were used to quantify the number of viable cells using Promega's CellTiter-Glo kit (G7570). Cholesterol luminescence values were normalized to cell viability and then a standard curve was used to obtain cholesterol concentration per sample ($\mu\text{mol}/\text{L}$).

Phospholipid Extraction and Measurement in Cells

2×10^6 SKMEL2 NT or *GRAMD1B* shRNA cells were pretreated in 4 $\mu\text{g}/\text{mL}$ dox-containing media for 4 days to induce *GRAMD1B* knockdown. On day 4, the cells were trypsinized, counted, and centrifuged to obtain cell pellets for phospholipid extractions. Extracts were suspended in 500 μL Abcam's phospholipid assay buffer and sonicated at an amplitude of 10%, with 10 total pulses of 1 second on ice. Samples were centrifuged for 10 minutes at 15,000 $\times g$ at 4°C and the supernatant was transferred to fresh tubes. Samples were diluted 1:5 in assay buffer and subject to Abcam's phospholipid assay kit as per manual instructions. A standard curve was used to calculate phospholipid levels in cells in pmol.

Membrane Fluidity Assay

SKMEL2 NT or *GRAMD1B* knockdown cells were pretreated in 4 $\mu\text{g}/\text{mL}$ dox-containing media for 4 days to induce *GRAMD1B* knockdown. On day 4, 10,000 cells were seeded in 96-well black plates. The next day, the assay was performed according to Abcam's membrane fluidity assay kit instructions. Excimer to monomer fluorescence was normalized to obtain relative membrane fluidity in these cells.

Cholesterol Extraction from Tumor Tissues and Blood

Adult male zebrafish ages 4- to 5-month-old were electroporated with plasmids as described before to generate NT and *gramd1b* KO melanomas. Animals were sacrificed 8 weeks after TEAZ, and blood was collected from 4 animals per condition using a previously described method (120) to assess blood cholesterol levels. Blood from animals was centrifuged at 21,000 $\times g$ for 1 minute, and the plasma supernatant was collected into fresh tubes for cholesterol analysis. Plasma was diluted 1:1,000 in Abcam's cholesterol assay buffer for the experiment. Simultaneously, melanomas were dissected from the same animals for tumor cholesterol experiments and extracted with 400 μL of chloroform:isopropanol:NP-40 (7:11:0.1). Extracts were sonicated at an amplitude of 10%, with 10 total pulses of 1 second. Extracts were centrifuged for 10 minutes at 15,000 $\times g$, and the organic phase was transferred to a new tube. Tubes were air dried at 55°C to remove chloroform. The samples were then dried in a speed-vac to remove the remaining organic solvent for 20 minutes. Dried lipids were resuspended with 400 μL of Cholesterol Assay Buffer by vortexing until homogeneous. Samples were further diluted 1:50 in Cholesterol Assay Buffer for the enzymatic assay. Abcam's cholesterol assay kit was then followed using manual instructions to measure total and free cholesterol in blood and tumor samples. A standard curve was used to calculate the concentration of cholesterol in samples.

Cholesterol Depletion Assay

On day 0, 100,000 NT or *GRAMD1B* shRNA SKMEL2 cells were pretreated in 4 $\mu\text{g}/\text{mL}$ dox-containing media in 6-well dishes to induce *GRAMD1B* knockdown for 48 hours. On day 2, cells were switched to either dox-containing control media (DMEM, 10% FBS, 1% antibiotics, 4 $\mu\text{g}/\text{mL}$ dox) or cholesterol depletion media (DMEM, 10% lipoprotein-free FBS, 1% antibiotics, 10 $\mu\text{mol}/\text{L}$ simvastatin, and 200 $\mu\text{mol}/\text{L}$ mevalonic acid, 4 $\mu\text{g}/\text{mL}$ dox) for another 48 hours. Because the mevalonate pathway is critical for cell viability, mevalonate supplementation was included in the cholesterol depletion mixture as done in Trinh and colleagues (121). On day 4, cholesterol depletion was confirmed through Promega's cholesterol Glo assay, and cells were seeded for invasion assays.

siRNA Knockdown Assays

On day 1, 3×10^6 melanoma cells were seeded in 10-cm dishes for siRNA experiments in antibiotic-free media using the Dharmafect transfection reagent as per manual instructions. Briefly, cells were transfected with 40 μ L siGENOME Control siRNA or *CYP27A1* siRNA and 40 μ L Dharmafect 1 per dish. The next day, the cells were replenished with fresh media containing antibiotics. Cells were harvested to seed for invasion assays and Western blot/real-time analysis 72 hours after transfection.

Dual Luciferase Assays

A375 or SKMEL2 cells (40×10^3) were seeded per well in 24-well plates in triplicate and transfected with a Renilla plasmid (40 ng), pGL3-AP-11 (400 ng), or pGL3-control plasmids (400 ng) per well using FuGENE HD (Promega) at a 3:1 FuGENE:DNA ratio. For sterol treatment assays, sterols were added at the time of transfection. For assays in shRNA cells, NT or *GRAMD1B* shRNA cells were pretreated in 4 μ g/mL dox for 48 hours and then seeded in 24-well plates in dox media and subjected to transfection. Luciferase activity was measured 48 hours after transfection using Promega's Dual Glo assay kit and a luminescence plate reader (Synergy). Firefly luciferase activity was normalized to Renilla luciferase activity to obtain relative luciferase levels per sample.

Statistics and Reproducibility

Statistical comparisons were performed with the aid of GraphPad Prism 8.4.3, and the statistical details including sample size and type of statistical test performed can be found in the figure legends. Statistical analysis was performed on data pooled from at least $n = 3$ independent experiments, with associated technical replicates per experiment. $P > 0.05$ is not considered statistically significant. *, $P < 0.05$; **, $P < 0.01$; ***, $P < 0.001$, and ****, $P < 0.0001$.

Data Availability

The code used to generate the plots in this paper is publicly available on GitHub (<https://github.com/Manikgarg/GRAMD1B-analysis>). The RNA-seq data generated in this study are uploaded to NCBI Gene Expression Omnibus and raw data as well as processed counts files are publicly available (accession number GSE202717). The Leeds Melanoma Cohort data (accession number EGAS00001002922) are available at the EGA. Plasmids will be available upon request. Normalized counts and results of DESEQ2 DE analysis and GSEA are listed in detail in Supplementary Tables S5–S7.

Authors' Disclosures

S. Suresh reports grants from the Melanoma Research Foundation, Memorial MSKCC TROT T32 training grant, Cycle for Survival, the Melanoma Research Alliance, The Debra and Leon Black Family Foundation, NIH Research Program Grants R01CA229215 and R01CA238317, NIH Director's New Innovator Award DP2CA186572, NCI Cancer Center Support Grant P30 CA08748, the Pershing Square Sohn Foundation, The Mark Foundation, the American Cancer Society, The Alan and Sandra Gerry Metastasis Research Initiative, the Harry J. Lloyd Foundation, Consano, the Starr Cancer Consortium, Wellcome Trust and CR-UK, the NIH Kirschstein-NRSA predoctoral fellowship F30CA254152, Medical Scientist Training Program grant from the NIH under award number T32GM007739, Predoctoral to Postdoctoral Fellow Transition Award (F99/K00) from the NIH under award number K00CA223016, CRUK (C588/A19167, C8216/A6129, C588/A10721), and the NIH (CA83115) during the conduct of the study. R. Rabbie reports other support from AstraZeneca outside the submitted work. R.M. White reports grants from the NIH, Cycle for Survival, the American Cancer Society, Pershing Square, The Mark Foundation, the Harry J. Lloyd Foundation, The Alan and Sandra

Gerry Metastasis Research Initiative at the Memorial Sloan Kettering Cancer Center, and the Starr Cancer Consortium during the conduct of the study, as well as personal fees from Qiagen/N-of-One outside the submitted work. No disclosures were reported by the other authors.

Authors' Contributions

S. Suresh: Conceptualization, resources, data curation, software, formal analysis, funding acquisition, validation, investigation, visualization, methodology, writing—original draft, project administration, writing—review and editing. **R. Rabbie:** Conceptualization, resources, data curation, software, formal analysis, investigation, visualization, methodology, writing—original draft, writing—review and editing. **M. Garg:** Resources, data curation, software, formal analysis, validation, investigation, visualization, methodology, writing—review and editing. **D. Lumaquin:** Data curation, software, formal analysis, investigation, visualization, methodology, writing—review and editing. **T.-S. Huang:** Resources, methodology, writing—review and editing. **E. Montal:** Software, formal analysis, investigation, visualization, methodology. **Y. Ma:** Data curation, software, formal analysis, investigation, visualization, writing—review and editing. **N.M. Cruz:** Conceptualization, formal analysis, methodology, writing—review and editing. **X. Tang:** Data curation, formal analysis, investigation, writing—review and editing. **J. Nsengimana:** Data curation, formal analysis, writing—review and editing. **J. Newton-Bishop:** Data curation, formal analysis, methodology. **M.V. Hunter:** Software, visualization, methodology, writing—review and editing. **Y. Zhu:** Formal analysis, investigation. **K. Chen:** Formal analysis, investigation. **E. de Stanchina:** Conceptualization, data curation, formal analysis, investigation, visualization, methodology, writing—review and editing. **D.J. Adams:** Conceptualization, resources, supervision, funding acquisition, visualization, methodology, project administration, writing—review and editing. **R.M. White:** Conceptualization, resources, supervision, funding acquisition, writing—original draft, project administration, writing—review and editing.

Acknowledgments

S. Suresh was supported by a Melanoma Research Foundation Career Development Award grant number 719502 and an MSKCC TROT T32 training grant T32 CA16000. D.J. Adams and R. Rabbie were supported by the Wellcome Trust and CR-UK. D. Lumaquin was supported by NIH Kirschstein-NRSA predoctoral fellowship F30CA254152. Y. Ma was supported by a Medical Scientist Training Program grant from the NIH under award number T32GM007739. E. Montal was supported by the Predoctoral to Postdoctoral Fellow Transition Award (F99/K00) from the NIH under award number K00CA223016. M. Garg was supported by an EMBL doctoral fellowship. We thank the Aquatics Core facility, Memorial Sloan Kettering Cancer Center, for their support in this work. We also thank members of the White lab for their advice in this work. We acknowledge the use of the Anti-tumor Assessment Core, Integrated Genomics Operation Core, funded by an NCI Cancer Center Support Grant (P30 CA08748). The Leeds Melanoma Cohort was funded by CRUK grants C588/A19167, C8216/A6129, an C588/A10721 and NIH grant CA83115.

The publication costs of this article were defrayed in part by the payment of publication fees. Therefore, and solely to indicate this fact, this article is hereby marked “advertisement” in accordance with 18 USC section 1734.

Note

Supplementary data for this article are available at Cancer Discovery Online (<http://cancerdiscovery.aacrjournals.org/>).

Received April 18, 2022; revised August 25, 2022; accepted October 14, 2022; published first October 19, 2022.

REFERENCES

- Kaufman CK, Mosimann C, Fan ZP, Yang S, Thomas AJ, Ablain J, et al. A zebrafish melanoma model reveals emergence of neural crest identity during melanoma initiation. *Science* 2016;351:aad2197.
- White RM, Cech J, Ratanasirintrao S, Lin CY, Rahl PB, Burke CJ, et al. DHODH modulates transcriptional elongation in the neural crest and melanoma. *Nature* 2011;471:518–22.
- Baggiolini A, Callahan SJ, Montal E, Weiss JM, Trieu T, Tagore MM, et al. Developmental chromatin programs determine oncogenic competence in melanoma. *Science* 2021;373:eabc1048.
- Shain AH, Bastian BC. From melanocytes to melanomas. *Nat Rev Cancer* 2016;16:345–58.
- Damsky WE, Theodosakis N, Bosenberg M. Melanoma metastasis: new concepts and evolving paradigms. *Oncogene* 2014;33:2413–22.
- CGA Network. Genomic classification of cutaneous melanoma. *Cell* 2015;161:1681–96.
- Hodis E, Watson IR, Kryukov GV, Arold ST, Imielinski M, Theurillat JP, et al. A landscape of driver mutations in melanoma. *Cell* 2012;150:251–63.
- Turajlic S, Furney SJ, Lambros MB, Mitsopoulos C, Kozarewa I, Geyer FC, et al. Whole genome sequencing of matched primary and metastatic acral melanomas. *Genome Res* 2012;22:196–207.
- Martincorena I, Roshan A, Gerstung M, Ellis P, Van Loo P, McLaren S, et al. Tumor evolution. High burden and pervasive positive selection of somatic mutations in normal human skin. *Science* 2015;348:880–6.
- Zhang M, Di Martino JS, Bowman RL, Campbell NR, Baksh SC, Simon-Vermot T, et al. Adipocyte-derived lipids mediate melanoma progression via FATP proteins. *Cancer Discov* 2018;8:1006–25.
- Nguyen B, Fong C, Luthra A, Smith SA, DiNatale RG, Nandakumar S, et al. Genomic characterization of metastatic patterns from prospective clinical sequencing of 25,000 patients. *Cell* 2022;185:563–75.
- Marzese DM, Scolyer RA, Huynh JL, Huang SK, Hirose H, Chong KK, et al. Epigenome-wide DNA methylation landscape of melanoma progression to brain metastasis reveals aberrations on homeobox D cluster associated with prognosis. *Hum Mol Genet* 2014;23:226–38.
- Shain AH, Joseph NM, Yu R, Benhamida J, Liu S, Prow T, et al. Genomic and transcriptomic analysis reveals incremental disruption of key signaling pathways during melanoma evolution. *Cancer Cell* 2018;34:45–55.
- Luke JJ, Ascierto PA, Carlino MS, Gershenwald JE, Grob JJ, Hauschild A, et al. KEYNOTE-716: phase III study of adjuvant pembrolizumab versus placebo in resected high-risk stage II melanoma. *Future Oncol* 2020;16:4429–38.
- Tarhini AA, Lee SJ, Hodi FS, Rao UNM, Cohen GI, Hamid O, et al. Phase III study of adjuvant ipilimumab (3 or 10 mg/kg) versus high-dose interferon alfa-2b for resected high-risk melanoma: North American intergroup E1609. *J Clin Oncol* 2020;38:567–75.
- Long GV, Hauschild A, Santinami M, Atkinson V, Mandalà M, Chiarion-Sileni V, et al. Adjuvant dabrafenib plus trametinib in stage III BRAF-mutated melanoma. *N Engl J Med* 2017;377:1813–23.
- Corrie PG, Marshall A, Dunn JA, Middleton MR, Nathan PD, Gore M, et al. Adjuvant bevacizumab in patients with melanoma at high risk of recurrence (AVAST-M): preplanned interim results from a multicentre, open-label, randomised controlled phase 3 study. *Lancet Oncol* 2014;15:620–30.
- Emmett MS, Symonds KE, Rigby H, Cook MG, Price R, Metcalfe C, et al. Prediction of melanoma metastasis by the Shields index based on lymphatic vessel density. *BMC Cancer* 2010;10:208.
- Faries MB, Wanek LA, Elashoff D, Wright BE, Morton DL. Predictors of occult nodal metastasis in patients with thin melanoma. *Arch Surg* 2010;145:137–42.
- Birkenfeld JS, Tucker-Schwartz JM, Soenksen LR, Avilés-Izquierdo JA, Marti-Fuster B. Computer-aided classification of suspicious pigmented lesions using wide-field images. *Comput Methods Programs Biomed* 2020;195:105631.
- Esteve A, Kuprel B, Novoa RA, Ko J, Swetter SM, Blau HM, et al. Dermatologist-level classification of skin cancer with deep neural networks. *Nature* 2017;542:115–8.
- Soenksen LR, Kassis T, Conover ST, Marti-Fuster B, Birkenfeld JS, Tucker-Schwartz J, et al. Using deep learning for dermatologist-level detection of suspicious pigmented skin lesions from wide-field images. *Sci Transl Med* 2021;13:eabb3652.
- Garg M, Couturier D-L, Nsengimana J, Fonseca NA, Wongchenko M, Yan Y, et al. Tumour gene expression signature in primary melanoma predicts long-term outcomes. *Nat Commun* 2021;12:1137.
- Thakur R, Laye JP, Lauss M, Diaz JMS, O'Shea SJ, Poźniak J, et al. Transcriptomic analysis reveals prognostic molecular signatures of stage I melanoma. *Clin Cancer Res* 2019;25:7424–35.
- Jönsson G, Busch C, Knappskog S, Geisler J, Miletic H, Ringnér M, et al. Gene expression profiling-based identification of molecular subtypes in stage IV melanomas with different clinical outcome. *Clin Cancer Res* 2010;16:3356–67.
- Gerami P, Cook RW, Russell MC, Wilkinson J, Amaria RN, Gonzalez R, et al. Gene expression profiling for molecular staging of cutaneous melanoma in patients undergoing sentinel lymph node biopsy. *J Am Acad Dermatol* 2015;72:780–5.
- Vetto JT, Hsueh EC, Gastman BR, Dillon LD, Monzon FA, Cook RW, et al. Guidance of sentinel lymph node biopsy decisions in patients with T1-T2 melanoma using gene expression profiling. *Future Oncol* 2019;15:1207–17.
- Gastman BR, Gerami P, Kurley SJ, Cook RW, Leachman S, Vetto JT. Identification of patients at risk of metastasis using a prognostic 31-gene expression profile in subpopulations of melanoma patients with favorable outcomes by standard criteria. *J Am Acad Dermatol* 2019;80:149–57.
- Ramaswamy S, Ross KN, Lander ES, Golub TR. A molecular signature of metastasis in primary solid tumors. *Nat Genet* 2003;33:49–54.
- Dhomen N, Reis-Filho JS, da Rocha Dias S, Hayward R, Savage K, Delmas V, et al. Oncogenic Braf induces melanocyte senescence and melanoma in mice. *Cancer Cell* 2009;15:294–303.
- Dankort D, Curley DP, Cartledge RA, Nelson B, Karnezis AN, Damsky WE, et al. Braf(V600E) cooperates with Pten loss to induce metastatic melanoma. *Nat Genet* 2009;41:544–52.
- Damsky WE, Curley DP, Santhanakrishnan M, Rosenbaum LE, Platt JT, Gould Rothberg BE, et al. β -catenin signaling controls metastasis in Braf-activated Pten-deficient melanomas. *Cancer Cell* 2011;20:741–54.
- Quintana E, Piskounova E, Shackleton M, Weinberg D, Eskiciok U, Fullen DR, et al. Human melanoma metastasis in NSG mice correlates with clinical outcome in patients. *Sci Transl Med* 2012;4:159ra149.
- Cho JH, Robinson JP, Arave RA, Burnett WJ, Kircher DA, Chen G, et al. AKT1 activation promotes development of melanoma metastases. *Cell Rep* 2015;13:898–905.
- Bok I, Vera O, Xu X, Jasani N, Nakamura K, Reff J, et al. A versatile ES cell-based melanoma mouse modeling platform. *Cancer Res* 2020;80:912–21.
- Callahan SJ, Tepan S, Zhang YM, Lindsay H, Burger A, Campbell NR, et al. Cancer modeling by transgene electroporation in adult zebrafish (TEAZ). *Dis Model Mech* 2018;11:dmm034561.
- Corrie PG, Marshall A, Nathan PD, Lorigan P, Gore M, Tahir S, et al. Adjuvant bevacizumab for melanoma patients at high risk of recurrence: survival analysis of the AVAST-M trial. *Ann Oncol* 2018;29:1843–52.
- Huang DW, Sherman BT, Lempicki RA. Bioinformatics enrichment tools: paths toward the comprehensive functional analysis of large gene lists. *Nucleic Acids Res* 2009;37:1–13.
- Huang DW, Sherman BT, Lempicki RA. Systematic and integrative analysis of large gene lists using DAVID bioinformatics resources. *Nat Protoc* 2009;4:44–57.
- Cerami E, Gao J, Dogrusoz U, Gross BE, Sumer SO, Aksoy BA, et al. The cBio cancer genomics portal: an open platform for exploring multidimensional cancer genomics data. *Cancer Discov* 2012;2:401–4.
- Patton EE, Widlund HR, Kutok JL, Kopani KR, Amatruda JF, Murphey RD, et al. BRAF mutations are sufficient to promote nevi formation and cooperate with p53 in the genesis of melanoma. *Curr Biol* 2005;15:249–54.
- Webster MR, Fane ME, Alicea GM, Basu S, Kossenkov AV, Marino GE, et al. Paradoxical role for wild-type p53 in driving therapy resistance in melanoma. *Mol Cell* 2020;77:633–44.

43. White RM, Sessa A, Burke C, Bowman T, LeBlanc J, Ceol C, et al. Transparent adult zebrafish as a tool for in vivo transplantation analysis. *Cell Stem Cell* 2008;2:183–9.
44. Ablain J, Xu M, Rothschild H, Jordan RC, Mito JK, Daniels BH, et al. Human tumor genomics and zebrafish modeling identify SPRED1 loss as a driver of mucosal melanoma. *Science* 2018;362:1055–60.
45. Ruzicka L, Howe DG, Ramachandran S, Toro S, Van Slyke CE, Bradford YM, et al. The zebrafish information network: new support for non-coding genes, richer gene ontology annotations and the alliance of genome resources. *Nucleic Acids Res* 2019;47:D867–73.
46. Sandhu J, Li S, Fairall L, Pfisterer SG, Gurnett JE, Xiao X, et al. Aster proteins facilitate nonvesicular plasma membrane to ER cholesterol transport in mammalian cells. *Cell* 2018;175:514–29.
47. Andersen J-P, Zhang J, Sun H, Liu X, Liu J, Nie J, et al. Aster-B coordinates with Arf1 to regulate mitochondrial cholesterol transport. *Mol Metab* 2020;42:101055.
48. Ercan B, Naito T, Koh DHZ, Dharmawan D, Saheki Y. Molecular basis of accessible plasma membrane cholesterol recognition by the GRAM domain of GRAMD1b. *EMBO J* 2021;40:e106524.
49. Rathore M, Girard C, Ohanna M, Tichet M, Ben Jouira R, Garcia E, et al. Cancer cell-derived long pentraxin 3 (PTX3) promotes melanoma migration through a toll-like receptor 4 (TLR4)/NF- κ B signaling pathway. *Oncogene* 2019;38:5873–89.
50. Huntington JT, Shields JM, Der CJ, Wyatt CA, Benbow U, Slingluff CL, et al. Overexpression of collagenase 1 (MMP-1) is mediated by the ERK pathway in invasive melanoma cells: role of BRAF mutation and fibroblast growth factor signaling. *J Biol Chem* 2004;279:33168–76.
51. Nikkola J, Vihinen P, Vlaykova T, Hahka-Kemppinen M, Kähäri V-M, Pyrhönen S. High expression levels of collagenase-1 and stromelysin-1 correlate with shorter disease-free survival in human metastatic melanoma. *Int J Cancer* 2002;97:432–8.
52. Braig S, Wallner S, Junglas B, Fuchshofer R, Bosserhoff AK. CTGF is overexpressed in malignant melanoma and promotes cell invasion and migration. *Br J Cancer* 2011;105:231–8.
53. Finger EC, Cheng CF, Williams TR, Rankin EB, Bedogni B, Tachiki L, et al. CTGF is a therapeutic target for metastatic melanoma. *Oncogene* 2014;33:1093–100.
54. Smirnova T, Bonapace L, MacDonald G, Kondo S, Wyckoff J, Ebersbach H, et al. Serpin E2 promotes breast cancer metastasis by remodeling the tumor matrix and polarizing tumor associated macrophages. *Oncotarget* 2016;7:82289–304.
55. Trinh MN, Brown MS, Seemann J, Vale G, McDonald JG, Goldstein JL, et al. Interplay between Asters/GRAMD1s and phosphatidylserine in intermembrane transport of LDL cholesterol. *Proc Natl Acad Sci U S A* 2022;119:e2120411119.
56. Naito T, Saheki Y. GRAMD1-mediated accessible cholesterol sensing and transport. *Biochim Biophys Acta Mol Cell Biol Lipids* 2021;1866:158957.
57. Höglinger D, Burgoyne T, Sanchez-Heras E, Hartwig P, Colaco A, Newton J, et al. NPC1 regulates ER contacts with endocytic organelles to mediate cholesterol egress. *Nat Commun* 2019;10:4276.
58. Brown MS, Goldstein JL. The SREBP pathway: regulation of cholesterol metabolism by proteolysis of a membrane-bound transcription factor. *Cell* 1997;89:331–40.
59. Kober DL, Radhakrishnan A, Goldstein JL, Brown MS, Clark LD, Bai XC, et al. Scap structures highlight key role for rotation of intertwined luminal loops in cholesterol sensing. *Cell* 2021;184:3689–701.
60. Kober DL, Xu S, Li S, Bajaj B, Liang G, Rosenbaum DM, et al. Identification of a degradation signal at the carboxy terminus of SREBP2: A new role for this domain in cholesterol homeostasis. *Proc Natl Acad Sci U S A* 2020;117:28080–91.
61. Goldstein JL, Brown MS. A century of cholesterol and coronaries: from plaques to genes to statins. *Cell* 2015;161:161–72.
62. Baek AE, Yu YRA, He S, Wardell SE, Chang CY, Kwon S, et al. The cholesterol metabolite 27-hydroxycholesterol facilitates breast cancer metastasis through its actions on immune cells. *Nat Commun* 2017;8:864.
63. Nelson ER, Wardell SE, Jasper JS, Park S, Suchindran S, Howe MK, et al. 27-Hydroxycholesterol links hypercholesterolemia and breast cancer pathophysiology. *Science* 2013;342:1094–8.
64. Wu Q, Ishikawa T, Sirianni R, Tang H, McDonald JG, Yuhanna IS, et al. 27-Hydroxycholesterol promotes cell-autonomous, ER-positive breast cancer growth. *Cell Rep* 2013;5:637–45.
65. Zhuang L, Kim J, Adam RM, Solomon KR, Freeman MR. Cholesterol targeting alters lipid raft composition and cell survival in prostate cancer cells and xenografts. *J Clin Invest* 2005;115:959–68.
66. Castellano BM, Thelen AM, Moldavski O, Feltes M, van der Welle REN, Mydock-McGrane L, et al. Lysosomal cholesterol activates mTORC1 via an SLC38A9-Niemann-Pick C1 signaling complex. *Science* 2017;355:1306–11.
67. Jiang S, Wang X, Song D, Liu X, Gu Y, Xu Z, et al. Cholesterol induces epithelial-to-mesenchymal transition of prostate cancer cells by suppressing degradation of EGFR through APMAP. *Cancer Res* 2019;79:3063–75.
68. Huang P, Nedelcu D, Watanabe M, Jao C, Kim Y, Liu J, et al. Cellular cholesterol directly activates smoothed hedgehog signaling. *Cell* 2016;166:1176–87.
69. DuSell CD, Umetani M, Shaul PW, Mangelsdorf DJ, McDonnell DP. 27-hydroxycholesterol is an endogenous selective estrogen receptor modulator. *Mol Endocrinol* 2008;22:65–77.
70. Campbell NR, Rao A, Hunter MV, Sznurkowska MK, Briker L, Zhang M, et al. Cooperation between melanoma cell states promotes metastasis through heterotypic cluster formation. *Dev Cell* 2021;56:2808–25.
71. Rambow F, Marine JC, Goding CR. Melanoma plasticity and phenotypic diversity: therapeutic barriers and opportunities. *Genes Dev* 2019;33:1295–318.
72. Hoek KS, Goding CR. Cancer stem cells versus phenotype-switching in melanoma. *Pigment Cell Melanoma Res* 2010;23:746–59.
73. Hoek KS, Eichhoff OM, Schlegel NC, Döbbling U, Kobert N, Schaerer L, et al. In vivo switching of human melanoma cells between proliferative and invasive states. *Cancer Res* 2008;68:650–6.
74. Falletta P, Sanchez-Del-Campo L, Chauhan J, Efferm M, Kenyon A, Kershaw CJ, et al. Translation reprogramming is an evolutionarily conserved driver of phenotypic plasticity and therapeutic resistance in melanoma. *Genes Dev* 2017;31:18–33.
75. Eichhoff OM, Zipser MC, Xu M, Weeraratna AT, Mihic D, Dummer R, et al. The immunohistochemistry of invasive and proliferative phenotype switching in melanoma: a case report. *Melanoma Res* 2010;20:349–55.
76. Verfaillie A, Imrichova H, Atak ZK, Dewaele M, Rambow F, Hulselmans G, et al. Decoding the regulatory landscape of melanoma reveals TEADs as regulators of the invasive cell state. *Nat Commun* 2015;6:6683.
77. Wouters J, Kalender-Atak Z, Minnoye L, Spanier KI, De Waegeneer M, Bravo González-Blas C, et al. Robust gene expression programs underlie recurrent cell states and phenotype switching in melanoma. *Nat Cell Biol* 2020;22:986–98.
78. Heinz S, Benner C, Spann N, Bertolino E, Lin YC, Laslo P, et al. Simple combinations of lineage-determining transcription factors prime cis-regulatory elements required for macrophage and B cell identities. *Mol Cell* 2010;38:576–89.
79. Weiss JM, Hunter MV, Cruz NM, Baggiolini A, Tagore M, Ma Y, et al. Anatomic position determines oncogenic specificity in melanoma. *Nature* 2022;604:354–61.
80. Eferl R, Wagner EF. AP-1: a double-edged sword in tumorigenesis. *Nat Rev Cancer* 2003;3:859–68.
81. Bhutiani N, Egger ME, McMasters KM. Optimizing follow-up assessment of patients with cutaneous melanoma. *Ann Surg Oncol* 2017;24:861–3.
82. Dercle L, Zhao B, Gönen M, Moskowitz CS, Firas A, Beylertig V, et al. Early readout on overall survival of patients with melanoma treated with immunotherapy using a novel imaging analysis. *JAMA Oncol* 2022;8:385–92.
83. Han D, Zager JS, Shyr Y, Chen H, Berry LD, Iyengar S, et al. Clinicopathologic predictors of sentinel lymph node metastasis in thin melanoma. *J Clin Oncol* 2013;31:4387–93.
84. Fisher NM, Schaffer JV, Berwick M, Bologna JL. Breslow depth of cutaneous melanoma: impact of factors related to surveillance of

- the skin, including prior skin biopsies and family history of melanoma. *J Am Acad Dermatol* 2005;53:393–406.
85. Pencheva N, Tran H, Buss C, Huh D, Drobnjak M, Busam K, et al. Convergent multi-miRNA targeting of ApoE drives LRP1/LRP8-dependent melanoma metastasis and angiogenesis. *Cell* 2012;151:1068–82.
 86. Tavazoie MF, Pollack I, Tanquero R, Ostendorf BN, Reis BS, Gonsalves FC, et al. LXR/ApoE activation restricts innate immune suppression in cancer. *Cell* 2018;172:825–40.
 87. Pencheva N, Buss CG, Posada J, Merghoub T, Tavazoie SF. Broad-spectrum therapeutic suppression of metastatic melanoma through nuclear hormone receptor activation. *Cell* 2014;156:986–1001.
 88. Ostendorf BN, Bilanovic J, Adaku N, Tafreshian KN, Tavora B, Vaughan RD, et al. Common germline variants of the human APOE gene modulate melanoma progression and survival. *Nat Med* 2020;26:1048–53.
 89. von Schuckmann LA, Khosrotehrani K, Ghiasvand R, Hughes MCB, van der Pols JC, Malt M, et al. Statins may reduce disease recurrence in patients with ulcerated primary melanoma. *Br J Dermatol* 2020;183:1049–55.
 90. Villa GR, Hulce JJ, Zanca C, Bi J, Ikegami S, Cahill GL, et al. An LXR-cholesterol axis creates a metabolic co-dependency for brain cancers. *Cancer Cell* 2016;30:683–93.
 91. Yue S, Li J, Lee SY, Lee HJ, Shao T, Song B, et al. Cholesteryl ester accumulation induced by PTEN loss and PI3K/AKT activation underlies human prostate cancer aggressiveness. *Cell Metab* 2014;19:393–406.
 92. Goldstein JL, DeBose-Boyd RA, Brown MS. Protein sensors for membrane sterols. *Cell* 2006;124:35–46.
 93. Bandara S, Ramkumar S, Imanishi S, Thomas LD, Sawant OB, Imanishi Y, et al. Aster proteins mediate carotenoid transport in mammalian cells. *Proc Natl Acad Sci U S A* 2022;119:e2200068119.
 94. Ng MYW, Charsou C, Lapao A, Singh S, Trachsel-Moncho L, Nakken S, et al. GRAMD1C regulates autophagy initiation and mitochondrial bioenergetics through ER-mitochondria cholesterol transport. *BioRxiv* 2021.08.04.455032 [Preprint]. 2021 [cited 2022 Aug 1]. Available from: <https://doi.org/10.1101/2021.08.04.455032>.
 95. Pikuleva IA, Babiker A, Waterman MR, Björkhem I. Activities of recombinant human cytochrome P450c27 (CYP27) which produce intermediates of alternative bile acid biosynthetic pathways. *J Biol Chem* 1998;273:18153–60.
 96. Cali JJ, Russell DW. Characterization of human sterol 27-hydroxylase: a mitochondrial cytochrome P-450 that catalyzes multiple oxidation reaction in bile acid biosynthesis. *J Biol Chem* 1991;266:7774–8.
 97. Luo M, Bao L, Chen Y, Xue Y, Wang Y, Zhang B, et al. ZMYND8 is a master regulator of 27-hydroxycholesterol that promotes tumorigenicity of breast cancer stem cells. *Sci Adv* 2022;8:eabn5295.
 98. Liu W, Chakraborty B, Safi R, Kazmin D, Chang C-Y, McDonnell DP. Dysregulated cholesterol homeostasis results in resistance to ferroptosis increasing tumorigenicity and metastasis in cancer. *Nat Commun* 2021;12:5103.
 99. Ma L, Vidana Gamage HE, Tiwari S, Han C, Henn MA, Krawczynska N, et al. The liver X receptor is selectively modulated to differentially alter female mammary metastasis-associated myeloid cells. *Endocrinology* 2022;163:bqac072.
 100. Umetani M, Ghosh P, Ishikawa T, Umetani J, Ahmed M, Mineo C, et al. The cholesterol metabolite 27-hydroxycholesterol promotes atherosclerosis via proinflammatory processes mediated by estrogen receptor alpha. *Cell Metab* 2014;20:172–82.
 101. Cheung E, Acevedo ML, Cole PA, Kraus WL. Altered pharmacology and distinct coactivator usage for estrogen receptor-dependent transcription through activating protein-1. *Proc Natl Acad Sci U S A* 2005;102:559–64.
 102. He H, Sinha I, Fan R, Haldosen L-A, Yan F, Zhao C, et al. c-Jun/AP-1 overexpression reprograms ER α signaling related to tamoxifen response in ER α -positive breast cancer. *Oncogene* 2018;37:2586–600.
 103. Khanna P, Lee JS, Sereemasapun A, Lee H, Baeg GH. GRAMD1B regulates cell migration in breast cancer cells through JAK/STAT and Akt signaling. *Sci Rep* 2018;8:9511.
 104. Pein M, Insua-Rodríguez J, Hongu T, Riedel A, Meier J, Wiedmann L, et al. Metastasis-initiating cells induce and exploit a fibroblast niche to fuel malignant colonization of the lungs. *Nat Commun* 2020;11:1494.
 105. Qian B-Z, Li J, Zhang H, Kitamura T, Zhang J, Campion LR, et al. CCL2 recruits inflammatory monocytes to facilitate breast-tumour metastasis. *Nature* 2011;475:222–5.
 106. Coffelt SB, de Visser KE. Cancer: inflammation lights the way to metastasis. *Nature* 2014;507:48–9.
 107. Gonzalez H, Hagerling C, Werb Z. Roles of the immune system in cancer: from tumor initiation to metastatic progression. *Genes Dev* 2018;32:1267–84.
 108. Robert C, Ribas A, Schachter J, Arance A, Grob JJ, Mortier L, et al. Pembrolizumab versus ipilimumab in advanced melanoma (KEY-NOTE-006): post-hoc 5-year results from an open-label, multicentre, randomised, controlled, phase 3 study. *Lancet Oncol* 2019;20:1239–51.
 109. Ablain J, Durand EM, Yang S, Zhou Y, Zon LI. A CRISPR/Cas9 vector system for tissue-specific gene disruption in zebrafish. *Dev Cell* 2015;32:756–64.
 110. Lumaquin D, Johns E, Montal E, Weiss JM, Ola D, Abuhashem A, et al. An in vivo reporter for tracking lipid droplet dynamics in transparent zebrafish. *eLife* 2021;10:e64744.
 111. Love MI, Huber W, Anders S. Moderated estimation of fold change and dispersion for RNA-seq data with DESeq2. *Genome Biol* 2014;15:550.
 112. Mi H, Muruganujan A, Huang X, Ebert D, Mills C, Guo X, et al. Protocol update for large-scale genome and gene function analysis with the PANTHER classification system (v.14.0). *Nat Protoc* 2019;14:703–21.
 113. Mi H, Ebert D, Muruganujan A, Mills C, Allou LP, Mushayamaha T, et al. PANTHER version 16: a revised family classification, tree-based classification tool, enhancer regions and extensive API. *Nucleic Acids Res* 2021;49:D394–403.
 114. Concordet JP, Haeussler M. CRISPOR: intuitive guide selection for CRISPR/Cas9 genome editing experiments and screens. *Nucleic Acids Res* 2018;46:W242–5.
 115. Heilmann S, Ratnakumar K, Langdon E, Kansler E, Kim I, Campbell NR, et al. A quantitative system for studying metastasis using transparent zebrafish. *Cancer Res* 2015;75:4272–82.
 116. Lindsay H, Burger A, Biyong B, Felker A, Hess C, Zaugg J, et al. CrisprVariants charts the mutation spectrum of genome engineering experiments. *Nat Biotechnol* 2016;34:701–2.
 117. Patro R, Duggal G, Love MI, Irizarry RA, Kingsford C. Salmon provides fast and bias-aware quantification of transcript expression. *Nat Methods* 2017;14:417–9.
 118. Subramanian A, Tamayo P, Mootha VK, Mukherjee S, Ebert BL, Gillette MA, et al. Gene set enrichment analysis: a knowledge-based approach for interpreting genome-wide expression profiles. *Proc Natl Acad Sci U S A* 2005;102:15545–50.
 119. Mootha VK, Lindgren CM, Eriksson KF, Subramanian A, Sihag S, Lehar J, et al. PGC-1 α -responsive genes involved in oxidative phosphorylation are coordinately downregulated in human diabetes. *Nat Genet* 2003;34:267–73.
 120. Babaei F, Ramalingam R, Tavendale A, Liang Y, Yan LSK, Ajuh P, et al. Novel blood collection method allows plasma proteome analysis from single zebrafish. *J Proteome Res* 2013;12:1580–90.
 121. Trinh MN, Brown MS, Goldstein JL, Han J, Vale G, McDonald JG, et al. Last step in the path of LDL cholesterol from lysosome to plasma membrane to ER is governed by phosphatidylserine. *Proc Natl Acad Sci U S A* 2020;117:18521–9.